European Journal of Mechanics A/Solids 48 (2014) 112–128

Contents lists available at ScienceDirect

European Journal of Mechanics A/Solids

journal homepage: www.elsevier.com/locate/ejmsol

Modeling and simulation of viscous electro-active polymers

Franziska Vogel [a], Serdar Göktepe [b], Paul Steinmann [a], Ellen Kuhl [c,*]

[a] Chair of Applied Mechanics, Friedrich-Alexander Universität Erlangen-Nürnberg (FAU), Egerlandstr. 5, 91058 Erlangen, Germany
[b] Department of Civil Engineering, Middle East Technical University, 06800 Ankara, Turkey
[c] Department of Mechanical Engineering, Stanford University, 496 Lomita Mall, Stanford, CA 94305-4040, USA

ARTICLE INFO

Article history:
Received 8 October 2013
Accepted 5 February 2014
Available online 12 March 2014

Keywords:
Electroactivity
Electrostatics
Electroelasticity
Viscoelasticity

ABSTRACT

Electro-active materials are capable of undergoing large deformation when stimulated by an electric field. They can be divided into electronic and ionic electro-active polymers (EAPs) depending on their actuation mechanism based on their composition. We consider electronic EAPs, for which attractive Coulomb forces or local re-orientation of polar groups cause a bulk deformation. Many of these materials exhibit pronounced visco-elastic behavior. Here we show the development and implementation of a constitutive model, which captures the influence of the electric field on the visco-elastic response within a geometrically non-linear finite element framework. The electric field affects not only the equilibrium part of the strain energy function, but also the viscous part. To adopt the familiar additive split of the strain from the small strain setting, we formulate the governing equations in the logarithmic strain space and additively decompose the logarithmic strain into elastic and viscous parts. We show that the incorporation of the electric field in the viscous response significantly alters the relaxation and hysteresis behavior of the model. Our parametric study demonstrates that the model is sensitive to the choice of the electro-viscous coupling parameters. We simulate several actuator structures to illustrate the performance of the method in typical relaxation and creep scenarios. Our model could serve as a design tool for micro-electro-mechanical systems, microfluidic devices, and stimuli-responsive gels such as artificial skin, tactile displays, or artificial muscle.

1. Introduction

The past two decades have seen an increasingly growing interest in smart materials that change their shape and their mechanical behavior in response to external non-mechanical stimuli. Prominent representatives of smart materials are electro-active polymers (EAPs), which react to the excitation by an electric field with a bulk deformation and a change in their material behavior. For good reasons, EAPs became popular as artificial muscles (Pelrine et al., 1998; Bar-Cohen, 2002, 2004) since they outperform classical actuators such as electro-magnetic motors, pneumatic systems, piezoelectrics or shape memory alloys within small-scale technologies in many ways (Pelrine et al., 2000a; O'Halloran et al., 2008; Brochu and Pei, 2010). Whenever low weight, production cost, operation frequency, fast response time or little available space are limiting factors, EAPs find their application within tunable and adaptive devices for a broad range of industries (Pelrine et al., 2000b, 2000a). Due to their flexibility in shape, EAPs have become an attractive design element in robotics, optics, acoustics and biomimetics (Pelrine et al., 1998, 2000b; Spencer, 1971) in a variety of actuator geometries (O'Halloran et al., 2008).

Depending on their actuation mechanism, EAPs can be divided into ionic and electronic electro-active polymers. Based on their distinct molecular structure, the transformation of electric energy into mechanical work is of different origin. Within ionic EAPs, local movement or diffusion of ions is responsible for the deformation; within electronic EAPs attractive Coulomb forces or local re-orientation of polar groups cause a bulk deformation. Field-induced Coulomb forces can either appear as intramolecular forces or as external force acting on dielectric elastomers coated with compliant electrodes. In this work, we consider electronic EAPs, without further specifying the underlying mechanism. The only restriction we make is to assume that the output stress varies at least quadratically with the electric field, a characteristic, which is often referred to as electrostrictive elastomers.

Since the EAPs under consideration consist of silicones, polyacrylics or polyurethanes, many of these materials exhibit a pronounced visco-elastic behavior (Johlitz et al., 2007; Wissler and

* Corresponding author.
E-mail address: ekuhl@stanford.edu (E. Kuhl).

http://dx.doi.org/10.1016/j.euromechsol.2014.02.001
0997-7538/

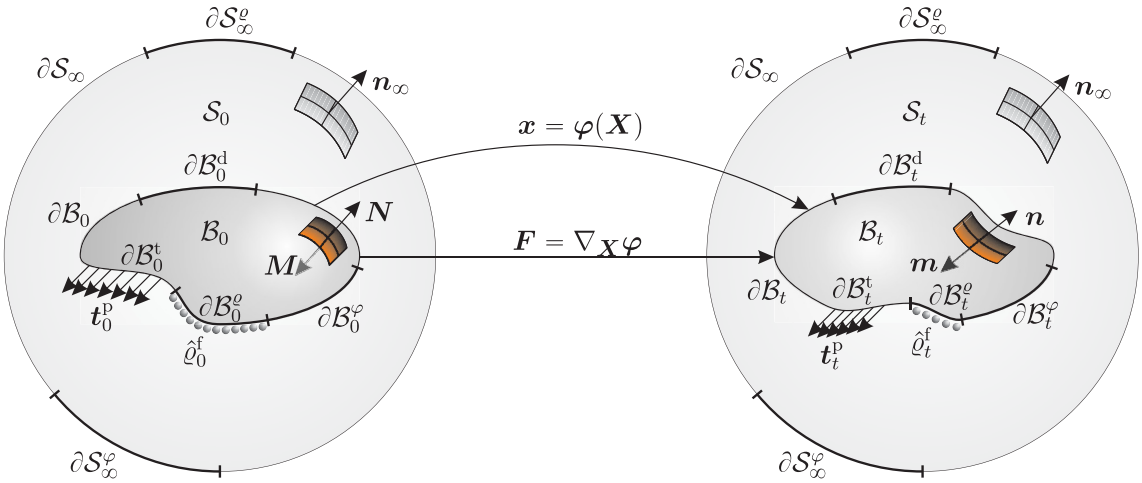

Fig. 1. Undeformed and deformed configuration of a nonlinearly deforming body immersed in free space.

Mazza, 2005; Brochu and Pei, 2010; Hossain et al., 2012). Here, we introduce a model, in which the electric field, governed by the electrostatic Maxwell equations, affects both the mechanical equilibrium equation and the viscous constitutive response. Typical applications are dielectric elastomers filled with particles to increase their electric permittivity (Mazzoldi et al., 2004), which were either fabricated in an electric field or are responsive to align with an electric field. A rotation of polar groups due to an externally applied electric field occurs in certain electrostrictive polymers (Brochu and Pei, 2010), which makes a consideration of the dielectric relaxation necessary (Khan et al., 2013).

We base our work on the well-established concepts within electro-elasticity (Dorfmann and Ogden, 2005, 2006; Bustamante et al., 2009) built on the original works (Toupin, 1956; Truesdell and Toupin, 1960; Eringen, 1963; Lax and Nelson, 1971; Tiersten, 1971; Maugin, 1977) and their advances in the last decade (Ericksen, 2007; Fosdick and Tang, 2007; McMeeking et al., 2007; Steigmann, 2009; Maugin, 2009). For the formulation of the viscous material model, we adopt the concept of internal variables to capture the dissipative effects (Simo and Hughes, 1998; Reese and Govindjee, 1998; Holzapfel, 2001). We assume an additive decomposition of the free energy density into equilibrium and viscous parts (Reese and Govindjee, 1998). For the definition of constitutive relations and a linear evolution equation to determine the internal variables, we work entirely in the logarithmic strain space. This concept was initially developed and applied in the context of plasticity (Miehe and Lamprecht, 2001; Miehe et al., 2002, 2009, 2011; Germain et al., 2010) and allows for an additive split in logarithmic elastic and viscous strains.

This special structure enables us to use a viscous rheological model, which originally stems from the geometric linear theory although we consider large deformations (El Sayed et al., 2008; Khan et al., 2013). Alternatively, we could adopt the multiplicative decomposition of the deformation gradient into elastic and viscous parts (Ask et al., 2012a, 2012b; Büschel et al., 2013). In contrast to the usage of internal variables, a functional thermodynamic framework of electro-visco-elasticity would also be possible (Chen, 2010).

The numerical implementation of the model is realized within a geometrically non-linear finite element framework (Vu et al., 2007). We simulate several actuator geometries, such as extending, bending and a diaphragm actuators, to show the performance of the method including typical relaxation and creep behavior. We perform a detailed parametric study that demonstrates the sensitivity of the model with regard to the choice of electro-viscous coupling parameters. We illustrate that the incorporation of the electric field into the viscous contribution significantly alters the relaxation and hysteresis behavior of the model.

2. Basic equations

The mathematical modeling of the mechanical elasticity problem coupled with electrostatics has been treated in detail from the early pioneering work (Toupin, 1956; ; Eringen, 1963; Lax and Nelson, 1971; Tiersten, 1971; Maugin, 1977) up to the present years (Ericksen, 2007; Fosdick and Tang, 2007; McMeeking et al., 2007; Steigmann, 2009; Maugin, 2009). Here we expand the formulations presented by Ogden and co-workers (Dorfmann and Ogden, 2005, 2006; Bustamante et al., 2009). To trace the origins, we briefly summarize the basic equations of nonlinear continuum mechanics and electrostatics.

2.1. Preliminaries

We investigate a nonlinearly deforming body $\mathcal{B}$ immersed in vacuum S, which is subject to an electric field as depicted in Fig. 1. Since the body may undergo large deformations, we distinguish between an undeformed configuration k^{v}_{1} and a deformed configuration $\mathcal{B}_t$. For the material and spatial setting, we divide the surface of the body in two different ways (Bustamante, 2009), to prescribe mechanical and electric boundary conditions:

$$\partial\mathcal{B}_0 = \partial\mathcal{B}^{\varrho}_0 \cup \partial\mathcal{B}^{\varphi}_0 = \partial\mathcal{B}^{\mathrm{d}}_0 \cup \partial\mathcal{B}^{\mathrm{t}}_0, \quad \partial\mathcal{B}_t = \partial\mathcal{B}^{\varrho}_t \cup \partial\mathcal{B}^{\varphi}_t = \partial\mathcal{B}^{\mathrm{d}}_t \cup \partial\mathcal{B}^{\mathrm{t}}_t \tag{1}$$

such that

$$\partial\mathcal{B}^{\varphi} \neq \varnothing, \quad \partial\mathcal{B}^{\varrho} \cap \partial\mathcal{B}^{\varphi} = \varnothing, \quad \partial\mathcal{B}^{\mathrm{d}} \cap \partial\mathcal{B}^{\mathrm{t}} = \varnothing \tag{2}$$

and

$$\partial\mathcal{S}_0 = \partial\mathcal{S}_{\infty} \cup \partial\mathcal{B}_0, \quad \partial\mathcal{S}_t = \partial\mathcal{S}_{\infty} \cup \partial\mathcal{B}_t \tag{3}$$

with

$$\partial\mathcal{S}_{\infty} = \partial\mathcal{S}^{\varrho}_{\infty} \cup \partial\mathcal{S}^{\varphi}_{\infty}, \quad \partial\mathcal{S}^{\varrho}_{\infty} \cap \partial\mathcal{S}^{\varphi}_{\infty} = \varnothing. \tag{4}$$

The boundary parts marked with the superscripts $^{\varrho}$ and $^{\varphi}$ denote the electric Neumann and Dirichlet boundaries, respectively, and the superscripts $^{\mathrm{d}}$ and $^{\mathrm{t}}$ denote their mechanical counterparts. We

assume the boundary ∂S_∞ to be far away from the boundary of the body $\partial\mathcal{B}$ and we assume homogeneous Dirichlet boundary conditions throughout, implying that it is unable to deform.

We distinguish the coordinates and the electric field quantities in the undeformed and deformed configurations by capital and small letters, respectively. Let φ denote the deformation map, $\boldsymbol{F}$ the deformation gradient, i.e., the derivative of φ with respect to the coordinates $\boldsymbol{X}$ in the material setting,

$$\boldsymbol{F} = \nabla_{\boldsymbol{X}}\varphi \tag{5}$$

and J is the determinant of $\boldsymbol{F}\cdot\nabla_{\boldsymbol{X}}$ is the nabla operator with respect to the material coordinates $\boldsymbol{X}$. The push-forward operations for the electric field quantities, the electric field $\mathbb{E}$, the dielectric displacement $\mathbb{D}$, and the polarization $\mathbb{P}$ read as (Maugin and Eringen, 1990)

$$\mathbb{e} = \mathbb{E}\cdot\boldsymbol{F}^{-1}, \quad \mathbb{d} = \mathbb{D}\cdot J^{-1}\boldsymbol{F}^{T}, \quad \mathbb{p} = \mathbb{P}\cdot J^{-1}\boldsymbol{F}^{T}. \tag{6}$$

In vacuum, the electric field and the dielectric displacement are coupled linearly via the permittivity of vacuum ε_0,

$$\mathbb{d} = \varepsilon_0\,\mathbb{e} =: \mathbb{d}^{\varepsilon} \quad \text{in } \mathcal{S}_t. \tag{7}$$

In the bulk, the relationship between the electric field and the dielectric displacement is typically nonlinear. Here we describe this nonlinearity with the help of an additional variable, the polarization $\mathbb{p}$

$$\mathbb{d} = \varepsilon_0\mathbb{e} + \mathbb{p} =: \mathbb{d}^{\varepsilon} + \mathbb{p} \quad \text{in } \mathcal{B}_t. \tag{8}$$

The referential free space electric displacement follows as $\mathbb{D}^{\varepsilon} = \varepsilon_0 J\boldsymbol{C}^{-1}\cdot\mathbb{E}$.

2.2. Electro-mechanical problem

We characterize the electrical problem through the electrostatic Maxwell equations and restrict ourselves to insulating materials without free currents and free electric charges. We specify the equations in the spatial configuration:

$$\nabla_{\boldsymbol{x}}\cdot\mathbb{d} = 0, \quad \text{in } \mathcal{B}_t\cup\mathcal{S}_t, \quad \text{and} \tag{9}$$

$$\nabla_{\boldsymbol{x}}\times\mathbb{e} = 0, \quad \text{in } \mathcal{B}_t\cup\mathcal{S}_t. \tag{10}$$

Eq. (10) is satisfied exactly by deriving the electric field from a scalar potential (Monk, 2003)

$$\mathbb{e} = -\nabla_{\boldsymbol{x}}\varphi, \quad \text{in } \mathcal{B}_t\cup\mathcal{S}_t. \tag{11}$$

In addition to the electric field equations, we solve the balance of linear momentum

$$\nabla_{\boldsymbol{x}}\cdot\boldsymbol{\sigma} + \boldsymbol{b}_t^{\text{pon}} + \boldsymbol{b}_t = \nabla_{\boldsymbol{x}}\cdot\boldsymbol{\sigma}^{\text{tot}} + \boldsymbol{b}_t = 0, \quad \text{in } \mathcal{B}_t, \tag{12}$$

where $\boldsymbol{b}_t^{\text{pon}}$ denotes the ponderomotive body force and $\boldsymbol{b}_t$ the mechanical body force. Here, $\boldsymbol{\sigma}^{\text{tot}}$ symbolizes a total Cauchy type symmetric stress tensor (Dorfmann and Ogden, 2005), which consists of a non-symmetric elastic Cauchy stress $\boldsymbol{\sigma}$ and the ponderomotive stress $\boldsymbol{\sigma}^{\text{pon}}$. $\boldsymbol{\sigma}^{\text{pon}}$ is defined such that (Bustamante et al., 2009)

$$\nabla_{\boldsymbol{x}}\cdot\boldsymbol{\sigma}^{\text{pon}} = \boldsymbol{b}_t^{\text{pon}} = \nabla_{\boldsymbol{x}}\,\mathbb{e}\cdot\mathbb{p}. \tag{13}$$

A split of the ponderomotive stress in non-symmetric and symmetric parts leads to the non-symmetric polarization stress (Steinmann, 2011)

$$\boldsymbol{\sigma}^{\text{pol}} = \mathbb{e}\otimes\mathbb{p}, \tag{14}$$

and the symmetric Maxwell stress

$$\boldsymbol{\sigma}^{\text{max}} = E_t\boldsymbol{i} + \varepsilon_0\mathbb{e}\otimes\mathbb{e}. \tag{15}$$

E_t is the free field electric energy density per spatial unit volume

$$E_t(\mathbb{e}) = -\frac{1}{2}\varepsilon_0\mathbb{e}\cdot\mathbb{e}. \tag{16}$$

Observe that the ordinary Cauchy stress $\boldsymbol{\sigma}$, the polarization stress $\boldsymbol{\sigma}^{\text{pol}}$ and the polarization $\mathbb{p}$ vanish outside matter. The Maxwell stress $\boldsymbol{\sigma}^{\text{max}}$ and the free space electric displacement $\mathbb{d}^{\varepsilon}$ exist, however, everywhere and both fulfill a divergence free condition. The Maxwell stress satisfies

$$\nabla_{\boldsymbol{x}}\cdot\boldsymbol{\sigma}^{\text{max}} = \boldsymbol{0}, \quad \text{in } \mathcal{S}_t. \tag{17}$$

To complete the boundary value problem, Dirichlet conditions are prescribed along the boundary $\partial\mathcal{B}_t^{\text{d}}$ for the deformation map $\boldsymbol{\varphi}$:

$$\varphi = \varphi^{p}, \quad \text{on } \partial\mathcal{B}_t^{d}. \tag{18}$$

The jump condition regarding the stress along the boundary of the body is given as in (Steinmann, 2011)

$$[\![\boldsymbol{\sigma}^{\text{tot}}]\!]\cdot\boldsymbol{n} = -\boldsymbol{t}_t^{\text{p}}, \quad \text{on } \partial\mathcal{B}_t^{\text{t}}, \tag{19}$$

where $\boldsymbol{t}_t^{\text{p}}$ are prescribed mechanical tractions and $\boldsymbol{n}$ is the normal vector to the surface of $\mathcal{B}_t$. For the electrical quantities we have to keep in mind that

$$[\![\mathbb{d}]\!]\cdot\boldsymbol{n} = \widehat{\varrho}_t^{\text{f}}, \quad \text{on } \partial\mathcal{B}_t^{\varrho}, \quad \text{and } \mathbb{d}\cdot\boldsymbol{n}_\infty = -\widehat{\varrho}_\infty^{\text{f}}, \quad \text{on } \partial\mathcal{S}_\infty^{\varrho}, \tag{20}$$

$$[\![\mathbb{e}]\!]\times\boldsymbol{n} = 0, \quad \text{on } \partial\mathcal{B}_t, \quad \text{and } \mathbb{e}\times\boldsymbol{n} = \mathbb{e}_\infty\times\boldsymbol{n}, \quad \text{on } \partial\mathcal{S}_\infty^{\varphi}, \tag{21}$$

where $\widehat{\varrho}_\infty^{\text{f}}$ is the density of free surface charges per undeformed area volume on the boundary at infinity, respectively. The boundary conditions for $\mathbb{e}$ (21) together with (11), lead to a continuity and a Dirichlet boundary conditions for the electric scalar potential

$$[\![\varphi]\!] = 0, \quad \text{on } \partial\mathcal{B}_t^{\varrho}, \quad \text{and } \varphi = \varphi_\infty, \quad \text{on } \partial\mathcal{S}_\infty^{\varphi}. \tag{22}$$

Furthermore, we can prescribe a value for the electric scalar potential along the interface

$$\varphi = \varphi^{\text{p}}, \quad \text{on } \partial\mathcal{B}_t^{\varphi}. \tag{23}$$

We conclude this section with a brief reminder of the aforementioned equations in the material configuration. A Piola transformation of $\boldsymbol{\sigma}^{\text{tot}}$ leads to a non-symmetric stress tensor $\boldsymbol{P}^{\text{tot}}$ in the undeformed configuration and the corresponding ponderomotive stresses

$$\boldsymbol{P}^{\text{tot}} = \boldsymbol{\sigma}^{\text{tot}}\cdot J\boldsymbol{F}^{-T}, \quad \boldsymbol{P}^{\text{pol}} = \mathbb{e}\otimes\mathbb{P}, \quad \boldsymbol{P}^{\text{max}} = E_0\boldsymbol{F}^{-T} + \mathbb{e}\otimes\mathbb{D}^{\varepsilon}. \tag{24}$$

E_0 is the material counterpart of E_t given by the identity $E_0 = JE_t$. Thus,

$$E_0(\boldsymbol{F},\mathbb{E}) = -\frac{1}{2}\varepsilon_0 J\boldsymbol{C}^{-1} : [\mathbb{E}\otimes\mathbb{E}]. \tag{25}$$

The transformations in (24) together with (6) allow a formulation of the set of equilibrium equations in the undeformed configuration (Dorfmann and Ogden, 2005):

$$\nabla_{\boldsymbol{X}}\cdot\boldsymbol{P}^{\mathrm{tot}}+\boldsymbol{b}_0=\boldsymbol{0},\quad \text{in } \mathcal{B}_0, \tag{26}$$

$$\nabla_{\boldsymbol{X}}\cdot\boldsymbol{P}^{\mathrm{max}}=\boldsymbol{0},\quad \text{in } \mathcal{S}_0, \tag{27}$$

$$\nabla_{\boldsymbol{X}}\cdot\mathbb{D}=0,\quad \text{in } \mathcal{B}_0\cup\mathcal{S}_0, \tag{28}$$

$$\nabla_{\boldsymbol{X}}\times\mathbb{E}=\boldsymbol{0},\quad \text{in } \mathcal{B}_0\cup\mathcal{S}_0, \tag{29}$$

(29) is equivalent to the existence of a scalar potential such that

$$\mathbb{E}=-\nabla_{\boldsymbol{X}}\varphi,\quad \text{in } \mathcal{B}_0\cup\mathcal{S}_0 \tag{30}$$

and the boundary conditions are translated to

$$[\![\boldsymbol{P}^{\mathrm{tot}}]\!]\cdot\boldsymbol{N}=-\boldsymbol{t}_0^{\mathrm{p}},\quad \text{on } \partial\mathcal{B}_0^{\mathrm{t}}, \tag{31}$$

$$[\![\mathbb{D}]\!]\cdot\boldsymbol{N}=\varrho_0^{\mathrm{f}},\quad \text{on } \partial\mathcal{B}_0^{\mathrm{e}}. \tag{32}$$

3. Material model for electro-visco-elasticity

We investigate a material model for electro-active material exhibiting viscous behavior. In our model, the electric field influences the equilibrium elastic response and the viscous behavior of the material at the same time. Thus, we consider mechanical and dielectric relaxation equally and develop a quite general model adjustable to all kinds of electro-active materials. We propose an electro-viscoelastic material model in the spirit of a transversely isotropic material. Thereby, we define the axis of anisotropy along the direction to the electric field $\mathbb{E}$. An imprinted preferred direction or re-orientation during electric stimulation of electric dipoles within an electro-active material motivates this approach. This can apply to dielectric elastomers filled with particles to increase their electric permittivity (Mazzoldi et al., 2004), whose curing process took place either under an electric field or for those, which consist of such a soft elastomeric matrix that the particles can align with the electric field. A rotation of polar groups due to an externally applied electric field occurs in certain electrostrictive polymers (Brochu and Pei, 2010), which makes a consideration of the dielectric relaxation necessary (Khan et al., 2013).

3.1. Constitutive relations derived from the dissipation inequality

To simplify the definition of the constitutive equations, we assume the existence of an amended, augmented, or total free energy (Dorfmann and Ogden, 2005, 2006)

$$W_0(\boldsymbol{F},\mathbb{E},\boldsymbol{Q}_1,\ldots,\boldsymbol{Q}_n)=\psi_0(\boldsymbol{F},\mathbb{E},\boldsymbol{Q}_1,\ldots,\boldsymbol{Q}_n)+E_0(\boldsymbol{F},\mathbb{E}), \tag{33}$$

depending on the deformation gradient $\boldsymbol{F}$, the electric field $\mathbb{E}$, and a set of the internal variables $\boldsymbol{Q}_1,\ldots,\boldsymbol{Q}_n$ for the incorporation of a viscous material model. The dissipation inequality based on (Pao, 1978; Maugin and Eringen, 1990; Dorfmann and Ogden, 2003) reads after a Legendre transformation (Bustamante et al., 2009; Khan et al., 2013) as

$$\mathcal{D}_0=\boldsymbol{P}^{\mathrm{tot}}:\dot{\boldsymbol{F}}-\mathbb{D}\cdot\dot{\mathbb{E}}-\dot{W}_0(\boldsymbol{F},\mathbb{E},\boldsymbol{Q}_1,\ldots,\boldsymbol{Q}_n)\geq 0. \tag{34}$$

Due to the additive split of W_0 into the strain energy function ψ_0 and the electric free field energy E_0, we can separate the derivatives of E_0 from the dissipation inequality and proceed directly to the constitutive relations for the Maxwell stress and the free space electric displacement:

$$\boldsymbol{P}^{\mathrm{max}}=\frac{\partial E_0(\boldsymbol{F},\mathbb{E})}{\partial\boldsymbol{F}},\quad \mathbb{D}^{\varepsilon}=-\frac{\partial E_0(\boldsymbol{F},\mathbb{E})}{\partial\mathbb{E}}. \tag{35}$$

To ensure the requirement of objectivity, we define the total energy in terms of $\boldsymbol{C}$. Furthermore, we assume our material to be isotropic and electro-mechanically coupled. Thus, we can express the strain energy density in terms of six invariants I_1 through I_6 corresponding to $\boldsymbol{C}$ and $\mathbb{E}\otimes\mathbb{E}$ (Spencer, 1971; Liu, 2002; Dorfmann and Ogden, 2005). With this at hand, we rewrite the dissipation inequality $\mathcal{D}_0'$ in terms of the Piola–Kirchhoff stress $\boldsymbol{S}$ and $\widetilde{\psi}_0$

$$\mathcal{D}_0'=\left[\boldsymbol{P}+\boldsymbol{P}^{\mathrm{pol}}\right]:\dot{\boldsymbol{F}}-\mathbb{P}\cdot\dot{\mathbb{E}}-\dot{\widetilde{\psi}}_0(\boldsymbol{F},\mathbb{E},\boldsymbol{Q}_1,\ldots,\boldsymbol{Q}_n) \tag{36}$$

$$=\frac{1}{2}\left[\boldsymbol{S}+\boldsymbol{S}^{\mathrm{pol}}\right]:\dot{\boldsymbol{C}}-\mathbb{P}\cdot\dot{\mathbb{E}}-\dot{\widetilde{\psi}}_0(\boldsymbol{C},\mathbb{E},\boldsymbol{Q}_1,\ldots,\boldsymbol{Q}_n)\geq 0. \tag{37}$$

$\widetilde{\psi}_0$ is the re-parameterization of ψ_0 such that

$$\begin{aligned}\widetilde{\psi}_0(\boldsymbol{C},\mathbb{E},\boldsymbol{Q}_1,\ldots,\boldsymbol{Q}_n)&=\widetilde{\psi}_0\left(\boldsymbol{F}^T\cdot\boldsymbol{F},\mathbb{E},\boldsymbol{Q}_1,\ldots,\boldsymbol{Q}_n\right)\\&=\psi_0(\boldsymbol{F},\mathbb{E},\boldsymbol{Q}_1,\ldots,\boldsymbol{Q}_n).\end{aligned} \tag{38}$$

For our desired material model, we combine two well-established principles encountered in visco-elasticity and plasticity: At first, we transfer to the logarithmic strain space and secondly, we use an extended generalized Maxwell model to represent the viscous material behavior.

The general concept roots in the definition of the logarithmic strain tensor

$$\boldsymbol{\varepsilon}=\frac{1}{2}\ln\boldsymbol{C}. \tag{39}$$

After a second re-parameterization of ψ_0 such that

$$\begin{aligned}\widehat{\psi}_0(\boldsymbol{\varepsilon},\mathbb{E},\boldsymbol{q}_1,\ldots,\boldsymbol{q}_n)&=\widehat{\psi}_0\left(\frac{1}{2}\ln\boldsymbol{C},\mathbb{E},\boldsymbol{q}_1,\ldots,\boldsymbol{q}_n\right)\\&=\widetilde{\psi}_0(\boldsymbol{C},\mathbb{E},\boldsymbol{Q}_1,\ldots,\boldsymbol{Q}_n),\end{aligned}$$

we can define the strain energy function in terms of the logarithmic strain ε, the electric field $\mathbb{E}$ and the corresponding internal variables $\boldsymbol{q}_1,\ldots\boldsymbol{q}_n$. Working in the logarithmic strain space mimics the small strain format (Miehe and Lamprecht, 2001; Miehe et al., 2002; Germain et al., 2010). This special structure enables us to use a rheological model for viscosity, which originally stems from the geometric linear theory although we consider large deformations.

The generalized Maxwell model in 1d consists of a single Hookean spring element with elastic modulus E^{∞} to represent the elastic equilibrium response in parallel to several Maxwell elements with elastic moduli E_1 through E_n to model the viscous response of the material (See Fig. 2). In order to extend the generalized Maxwell model to the coupled electro-mechanical 3d problem, we propose that the energy stored within the springs depends on the strain and the electric field. This approach is applied to the equilibrium spring and to the springs in the viscous branches. In 1d, this translates to Young's moduli $E^{\infty}(\mathbb{E}),E_1(\mathbb{E}),\ldots,E_n(\mathbb{E})$ that depend on the electric field.

We pursue a decoupled representation of the strain energy density $\widehat{\psi}_0$ (Reese and Govindjee, 1998; Holzapfel, 2001) and split $\widehat{\psi}_0$ additively into an equilibrium part $\widehat{\psi}_0^{\infty}$ and a viscous part $\widehat{\psi}_0^{\nu}$. The equilibrium part $\widehat{\psi}_0^{\infty}$ represents the strain energy density in the electro-elastic Hooke element and $\widehat{\psi}_0^{\nu}$ the energy in the electro-viscous Maxwell elements:

$$\widehat{\psi}_0(\boldsymbol{\varepsilon},\mathbb{E},\boldsymbol{q}_1,\ldots,\boldsymbol{q}_n)=\widehat{\psi}_0^{\infty}(\boldsymbol{\varepsilon},\mathbb{E})+\widehat{\psi}_0^{\nu}(\boldsymbol{\varepsilon},\mathbb{E},\boldsymbol{q}_1,\ldots,\boldsymbol{q}_n). \tag{40}$$

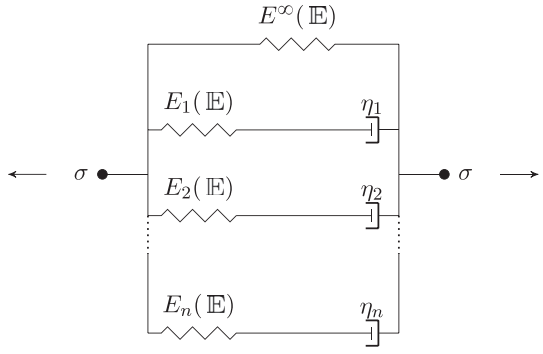

Fig. 2. Generalized Maxwell model for the one dimensional case with one Hookean spring element and n Maxwell elements in parallel.

In the state of thermodynamical equilibrium, the springs of the Maxwell elements are relaxed and the total energy density consists only of the equilibrium part $\widehat{\psi_0}^{\infty}$.

The total logarithmic strain ε corresponds to the elongation of the equilibrium spring. As a special consequence of the linear theory, the total strain can be split for each Maxwell element in the elastic logarithmic strain ε^e corresponding to the elongation of the spring and in the viscous logarithmic strain ε^v corresponding to the elongation of the dashpot. The resulting identity

$$\boldsymbol{\varepsilon} = \boldsymbol{\varepsilon}_i^e + \boldsymbol{\varepsilon}_i^v \quad \forall\ i \in \{1,\dots,n\} \tag{41}$$

motivates the identification of the internal variable $\boldsymbol{q}_i$ with the viscous logarithmic strain $\boldsymbol{\varepsilon}_i^v$ within the i^{th} Maxwell element (Reese and Govindjee, 1998;). A formal change of the input variables leads to a strain energy function of the form

$$\widehat{\psi_0}(\boldsymbol{\varepsilon},\mathbb{E},\boldsymbol{\varepsilon}_1^v,\dots,\boldsymbol{\varepsilon}_n^v) = \widehat{\psi_0}^{\infty}(\boldsymbol{\varepsilon},\mathbb{E}) + \widehat{\psi_0}^{v}(\boldsymbol{\varepsilon},\mathbb{E},\boldsymbol{\varepsilon}_1^v,\dots,\boldsymbol{\varepsilon}_n^v). \tag{42}$$

In a final step, we transfer the pair of work conjugates $(\boldsymbol{S}+\boldsymbol{S}^{\text{pol}},\boldsymbol{C})$ from Eq. (37) to the logarithmic strain setting. For doing so, we introduce a fourth order transformation tensor

$$P = 2\frac{\partial \boldsymbol{\varepsilon}}{\partial \boldsymbol{C}}, \tag{43}$$

and a logarithmic analog to the Piola–Kirchhoff stress

$$\boldsymbol{S}_{\log} + \boldsymbol{S}_{\log}^{\text{pol}} := \left[\boldsymbol{S} + \boldsymbol{S}^{\text{pol}}\right] : P^{-1}. \tag{44}$$

Rewriting $\dot{\boldsymbol{C}}$ in terms of P and ε, modifies the dissipation inequality (37) to

$$\mathcal{D}_0'' = \left[\boldsymbol{S}_{\log} + \boldsymbol{S}_{\log}^{\text{pol}}\right] : \dot{\varepsilon} - \mathbb{P}\cdot\dot{\mathbb{E}} - \dot{\widehat{\psi_0}}(\varepsilon,\mathbb{E},\varepsilon_1^v,\dots,\varepsilon_n^v) \geq 0. \tag{45}$$

From here, we derive constitutive relations with the help of the Coleman–Noll procedure

$$\boldsymbol{S}_{\log} + \boldsymbol{S}_{\log}^{\text{pol}} = \frac{\partial \widehat{\psi_0}(\varepsilon,\mathbb{E},\varepsilon_1^v,\dots,\varepsilon_n^v)}{\partial \varepsilon}, \quad \mathbb{P} = -\frac{\partial \widehat{\psi_0}(\varepsilon,\mathbb{E},\varepsilon_1^v,\dots,\varepsilon_n^v)}{\partial \mathbb{E}}. \tag{46}$$

Using the additive split of the strain energy density in (40), we can define a separation of the stress tensor $\boldsymbol{S}_{\log}+\boldsymbol{S}_{\log}^{\text{pol}}$ and $\mathbb{P}$ in equilibrium and viscous parts:

$$\boldsymbol{S}_{\log}^{\infty} = \left[\boldsymbol{S}_{\log}+\boldsymbol{S}_{\log}^{\text{pol}}\right]^{\infty} = \frac{\partial \widehat{\psi_0}^{\infty}(\varepsilon,\mathbb{E})}{\partial \varepsilon}, \quad \boldsymbol{S}_{\log}^{v} = \left[\boldsymbol{S}_{\log}+\boldsymbol{S}_{\log}^{\text{pol}}\right]^{v} = \frac{\partial \widehat{\psi_0}^{v}(\varepsilon,\mathbb{E},\varepsilon_1^v,\dots,\varepsilon_n^v)}{\partial \varepsilon}, \tag{47}$$

$$\mathbb{P}^{\infty} = -\frac{\partial \widehat{\psi_0}^{\infty}(\varepsilon,\mathbb{E})}{\partial \mathbb{E}}, \quad \mathbb{P}^{v} = -\frac{\partial \widehat{\psi_0}^{v}(\varepsilon,\mathbb{E},\varepsilon_1^v,\dots,\varepsilon_n^v)}{\partial \mathbb{E}}. \tag{48}$$

The remaining reduced dissipation inequality for the logarithmic viscous strain reads as

$$\mathcal{D}_0^{\text{red}} = -\sum_{i=1}^{n} \frac{\partial \widehat{\psi_0}^{v}(\varepsilon,\mathbb{E},\varepsilon_1^v,\dots,\varepsilon_n^v)}{\partial \varepsilon_i^v} : \dot{\varepsilon}_i^v \geq 0. \tag{49}$$

3.2. Explicit choice for the energy density functions

We consider a generalized Maxwell model with n independent Maxwell elements arranged in parallel. Thus, we can define a strain energy function $\widehat{\psi_{0,i}}^{v}$ for each Maxwell element separately, which sum up to the viscous strain energy $\widehat{\psi_0}^{v}$:

$$\widehat{\psi_0}^{v}(\varepsilon,\mathbb{E},\varepsilon_1^v,\dots\varepsilon_n^v) = \sum_{i}^{n} \widehat{\psi_{0,i}}^{v}(\varepsilon,\mathbb{E},\varepsilon_i^v). \tag{50}$$

As in the small deformation regime, $\widehat{\psi_0}^{\infty}$ and $\widehat{\psi_{0,i}}^{v}$ are quadratic functions in the total logarithmic strain ε and the elastic logarithmic strain ε_i^e (Reese and Govindjee, 1998; Holzapfel, 2001), respectively. With Eq. (41), we can express this directly as

$$\widehat{\psi_0}^{\infty}(\varepsilon,\mathbb{E}) = \frac{1}{2}\varepsilon : \mathrm{E}^4(\mathbb{E}) : \varepsilon + c_1 \boldsymbol{I} : \mathbb{E}\otimes\mathbb{E} + c_2\varepsilon : \mathbb{E}\otimes\mathbb{E}, \tag{51}$$

$$\widehat{\psi_{0,i}}^{v}(\varepsilon,\mathbb{E},\varepsilon_i^v) = \frac{1}{2}[\varepsilon-\varepsilon_i^v] : E^{4,\mathrm{v}}(\mathbb{E}) : [\varepsilon-\varepsilon_i^v] \quad \forall i \in \{1,\dots,n\}. \tag{52}$$

Besides the quadratic term in the logarithmic strains, we amended the equilibrium energy $\widehat{\psi_0}^{\infty}$ by two terms corresponding to the invariants $I_4 = \boldsymbol{I} : \mathbb{E}\otimes\mathbb{E}$ and $I_5 = \boldsymbol{C} : \mathbb{E}\otimes\mathbb{E}$, which are responsible for the polarization and the electrostrictive effect (Maugin and Eringen, 1990), respectively. The coupling parameters have to fulfill the conditions $c_1 < 0$ and $c_2 > 0$ to guarantee a reasonable orientation of $\mathbb{D}$ in comparison to $\mathbb{E}$ and a contraction of the material within the direction of $\mathbb{E}$.

We use here the definition of the transversely isotropic fourth-order tensor $\mathrm{E}^4(\mathbb{E})$

$$\begin{aligned}\mathrm{E}^4(\mathbb{E}) := {} & k_1^e \boldsymbol{I}\otimes\boldsymbol{I} + k_2^e\, \mathbb{1}_{sym}^4 + k_3^e[\boldsymbol{I}\otimes\boldsymbol{\kappa} + \boldsymbol{\kappa}\otimes\boldsymbol{I}] \\ & + k_4^e \boldsymbol{\kappa}\otimes\boldsymbol{\kappa} + k_5^e\left[\boldsymbol{I}\overline{\otimes}\boldsymbol{\kappa} + \boldsymbol{I}\underline{\otimes}\boldsymbol{\kappa} + \boldsymbol{\kappa}\overline{\otimes}\boldsymbol{I} + \boldsymbol{\kappa}\underline{\otimes}\boldsymbol{I}\right]\end{aligned} \tag{53}$$

with the anisotropic (structural) tensor $\boldsymbol{\kappa} = \mathbb{E}\otimes\mathbb{E}$. $E^{4,\mathrm{v}}$ follows the same definition with its constants k_1^v through k_5^v. To clarify notation, we used the non-standard dyadic products of any two second order tensor: $\boldsymbol{A}\overline{\otimes}\boldsymbol{B} = A_{ik}B_{jl}\boldsymbol{e_i}\otimes\boldsymbol{e_j}\otimes\boldsymbol{e_k}\otimes\boldsymbol{e_l}$ and $\boldsymbol{A}\underline{\otimes}\boldsymbol{B} = A_{il}B_{jk}\boldsymbol{e_i}\otimes\boldsymbol{e_j}\otimes\boldsymbol{e_k}\otimes\boldsymbol{e_l}$. With this, the symmetric fourth order unit tensor reads as $\mathbb{1}_{sym}^4 = \frac{1}{2}[\boldsymbol{I}\overline{\otimes}\boldsymbol{I} + \boldsymbol{I}\underline{\otimes}\boldsymbol{I}]$.

3.3. Evolution equation for the internal variables

Comparing the derivatives of the viscous strain energy function Eq. (52) with respect to the logarithmic strain tensors, leads to the identity

$$-\frac{\partial \widehat{\psi_{0,i}}^{\nu}(\varepsilon,\mathbb{E},\varepsilon_i^{\nu})}{\partial \varepsilon_i^{\nu}} = \frac{\partial \widehat{\psi_{0,i}}^{\nu}(\varepsilon,\mathbb{E},\varepsilon_i^{\nu})}{\partial \varepsilon} =: \boldsymbol{S}_{\log,i}^{\nu} \quad \forall i \in \{1,\dots,n\}. \tag{54}$$

This allows for a manipulation of the reduced dissipation inequality (49) to

$$\boldsymbol{S}_{\log,i}^{\nu} : \dot{\varepsilon}_i^{\nu} \geq 0 \quad \forall\ i \in \{1,\dots,n\}, \tag{55}$$

where $\boldsymbol{S}_{\log,i}^{\nu}$ is the stress acting on the dashpot in the i^{th} Maxwell element with viscosity parameter η_i. We assume here a linear relationship between the stress $\boldsymbol{S}_{\log,i}^{\nu}$ and the rate of strain $\dot{\varepsilon}_i^{\nu}$ in order to fulfill the non-negativity condition (55) of the dissipation function (Simo and Hughes, 1998):

$$\boldsymbol{S}_{\log,i}^{\nu} = \eta_i \dot{\varepsilon}_i^{\nu} = E_i^{4,\nu}(\mathbb{E}) : [\varepsilon - \varepsilon_i^{\nu}] \quad \forall\ i \in \{1,\dots,n\}. \tag{56}$$

This leads to a linear evolution equation for the logarithmic viscous strain, which we discretize by a backward Euler scheme. The update formula at time step t_{k+1} for $k \geq 0$ reads as:

$$\dot{\varepsilon}^{\nu} \approx \frac{\varepsilon_{k+1,i}^{\nu} - \varepsilon_{k,i}^{\nu}}{\Delta t} \overset{!}{=} \frac{1}{\eta_i} E_i^{4,\nu}(\mathbb{E}_{k+1}) : [\varepsilon_{k+1} - \varepsilon_{k+1,i}^{\nu}] \ \forall\ i \in \{1,\dots,n\}, \tag{57}$$

where $\Delta t = t_{k+1} - t_k$. Solving this equation for the updated viscous logarithmic strain renders

$$\varepsilon_{k+1,i}^{\nu} = \mathbb{A}_i^{-1} : \left[\varepsilon_{k,i}^{\nu} + \frac{\Delta t}{\eta_i} E_i^{4,\nu}(\mathbb{E}_{k+1}) : \varepsilon_{k+1}\right] \tag{58}$$

with $\mathbb{A}_i := \mathbb{1}_{sym}^4 + \frac{\Delta t}{\eta_i} E_i^{4,\nu}(\mathbb{E}_{k+1})$.

4. Weak form and its linearization

We want to solve the boundary value problem (9)–(12) in a weak sense and are looking for a pair of solutions $(\boldsymbol{\varphi},\varphi)$ in the function spaces

$$\mathcal{U}_{\boldsymbol{\varphi}}(\mathcal{B}_t \cup \mathcal{S}_t) = \left\{\boldsymbol{u} \in \mathrm{H}^1(\mathcal{B}_t \cup \mathcal{S}_t) \,\middle|\, \boldsymbol{u}|_{\partial\mathcal{B}_t^{\mathrm{d}}} = \varphi^{\mathrm{P}}, \quad \boldsymbol{u}|_{\partial\mathcal{S}_\infty} = \boldsymbol{X}\right\},$$

$$\mathcal{V}_{\boldsymbol{\varphi}}(\mathcal{B}_t \cup \mathcal{S}_t) = \left\{v \in \mathrm{H}^1(\mathcal{B}_t \cup \mathcal{S}_t) \,\middle|\, v|_{\partial\mathcal{B}_t^{\varphi}} = \varphi^{\mathrm{P}}, \quad v|_{\partial\mathcal{S}_\infty^{\varphi}} = \varphi_\infty\right\},$$

in order to fulfill the Dirichlet boundary conditions (18), (22) and (23) a priori. To obtain the weak form, we multiply Eq. (9) and (12) with test functions $(\delta\boldsymbol{\varphi},\delta\varphi)$ from the functional spaces

$$\mathcal{U}_0(\mathcal{B}_0 \cup \mathcal{S}_0) = \left\{\boldsymbol{u} \in \mathrm{H}^1(\mathcal{B}_0 \cup \mathcal{S}_0) | \quad \boldsymbol{u}|_{\partial\mathcal{B}_0^{\mathrm{d}}} 0, \quad \boldsymbol{u}|_{\partial\mathcal{S}_\infty} = \boldsymbol{0}\right\},$$

$$\mathcal{V}_0(\mathcal{B}_0 \cup \mathcal{S}_0) = \left\{v \in \mathrm{H}^1(\mathcal{B}_0 \cup \mathcal{S}_0) | \quad v|_{\partial\mathcal{B}_0^{\varphi}} 0, \quad v|_{\partial\mathcal{S}_0^{\varphi}} = 0\right\}.$$

After a partial integration and insertion of the boundary conditions, the weak form of the problem reads as follows

$$\begin{aligned} 0 = & \int_{\mathcal{B}_t \cup \mathcal{S}_t} \boldsymbol{\sigma}^{\max} : \nabla_{\boldsymbol{x}} \delta\varphi + \mathbb{d}^{\varepsilon} \cdot \nabla_{\boldsymbol{x}} \delta\varphi \,\mathrm{dv} \\ & + \int_{\mathcal{B}_t} \left[\boldsymbol{\sigma} + \boldsymbol{\sigma}^{\mathrm{pol}}\right] : \nabla_{\boldsymbol{x}} \delta\varphi + \mathbb{p} \cdot \nabla_{\boldsymbol{x}} \delta\varphi \,\mathrm{dv} \\ & - \int_{\mathcal{B}_t} \boldsymbol{b}_t \cdot \delta\varphi \,\mathrm{dv} - \int_{\partial\mathcal{B}_t} \boldsymbol{t}_t^{\mathrm{p}} \cdot \delta\varphi \,\mathrm{da} + \int_{\partial\mathcal{B}_t^{\varphi}} \widehat{\varrho}_t^{\mathrm{f}} \delta\varphi \,\mathrm{da} \\ & + \int_{\partial\mathcal{S}_\infty^{\varphi}} \widehat{\varrho}_\infty^{\mathrm{f}} \delta\varphi \,\mathrm{da}. \end{aligned} \tag{59}$$

4.1. Internal virtual work

The transformation to the logarithmic strain space makes some modifications in the internal virtual work necessary. For the sake of brevity, we will concentrate here on the internal work inside the body. The derivation for the surrounding free space can be obtained analogously. For the investigation of the external contribution we refer to standard text books (Wriggers, 2001; Belytschko et al., 2000). The term under consideration reduces to

$$\begin{aligned} g_{\mathrm{int}}(\boldsymbol{\varphi},\varphi,\delta\boldsymbol{\varphi},\delta\varphi) = & \int_{\mathcal{B}_t} \boldsymbol{\sigma}^{\max} : \nabla_{\boldsymbol{x}} \delta\boldsymbol{\varphi} + \mathbb{d}^{\varepsilon} \cdot \nabla_{\boldsymbol{x}} \delta\varphi + \left[\boldsymbol{\sigma} + \boldsymbol{\sigma}^{\mathrm{pol}}\right] \\ & : \nabla_{\boldsymbol{x}} \delta\boldsymbol{\varphi} + \mathbb{p} \cdot \nabla_{\boldsymbol{x}} \delta\varphi \,\mathrm{dv}. \end{aligned} \tag{60}$$

The Maxwell stress $\boldsymbol{\sigma}^{\max}$ and the free space electric displacement $\mathbb{d}^{\varepsilon}$ are implicitly given by the material constitutive relations (35) or explicitly in (15) and (8). For the remaining stress contribution $\boldsymbol{\sigma} + \boldsymbol{\sigma}^{\mathrm{pol}}$ and the polarization $\mathbb{p}$, we exploit the additive decomposition of the strain energy function $\widehat{\psi}_0$ to split both into equilibrium and viscous parts. With the transformation $\boldsymbol{\sigma} + \boldsymbol{\sigma}^{\mathrm{pol}} = J^{-1}\boldsymbol{F} \cdot [\boldsymbol{S} + \boldsymbol{S}^{\mathrm{pol}}] \cdot \boldsymbol{F}^T$, (44) and the constitutive relation (47), it follows that

$$\begin{aligned} \boldsymbol{\sigma} + \boldsymbol{\sigma}^{\mathrm{pol}} &= J^{-1}\boldsymbol{F} \cdot [[\boldsymbol{S}_{\log}^{\infty} + \boldsymbol{S}_{\log}^{\nu}] : \mathrm{P}] \cdot \boldsymbol{F}^T \\ &= J^{-1}\boldsymbol{F} \cdot \left[\left[\varepsilon : \mathrm{E}^4(\mathbb{E}) + [\varepsilon - \varepsilon^{\nu}] : \mathrm{E}^{4,\nu}(\mathbb{E})\right] : P\right] \cdot \boldsymbol{F}^T. \end{aligned} \tag{61}$$

For the polarization we exploit the push-forward operation (6.3) and the constitutive relation (48) for the material configuration to end up with

$$\mathbb{p} = -\frac{1}{2} J^{-1} \left[\varepsilon : \mathrm{d}_{\mathbb{E}} E^4(\mathbb{E}) \overset{34}{:} \varepsilon + [\varepsilon - \varepsilon^{\nu}] : \mathrm{d}_{\mathbb{E}} \mathrm{E}^{4,\nu}(\mathbb{E}) \overset{34}{:} [\varepsilon - \varepsilon^{\nu}]\right] \cdot \boldsymbol{F}^T. \tag{62}$$

The double contraction in explicit form reads as

$$\varepsilon : \mathrm{d}_{\mathbb{E}} \mathrm{E}^4(\mathbb{E}) \overset{34}{:} \varepsilon \cdot \boldsymbol{F}^T = 2[k_3 \mathrm{tr}\varepsilon + k_4[\varepsilon : \mathbb{E} \otimes \mathbb{E}]][\boldsymbol{F} \cdot \varepsilon \cdot \mathbb{E}] + 4k_5[\boldsymbol{F} \cdot \varepsilon \cdot \varepsilon \cdot \mathbb{E}]. \tag{63}$$

4.2. Linearization and consistent tangent moduli

In view of solving the governing equations numerically with a Newton–Raphson method, we linearize the weak form (59) with respect to the unknown fields $(\boldsymbol{\varphi},\varphi)$. This calls for a variation of the weak form, which we show here in detail for selected terms of the internal virtual work. We derive the variation in material configuration and then we perform a push-forward to spatial configuration:

$$\begin{aligned} \Delta g_{\mathrm{int}}(\boldsymbol{\varphi},\varphi,\delta\boldsymbol{\varphi},\delta\varphi) = & \int_{\mathcal{B}_t} J^{-1}[\nabla_{\boldsymbol{x}}\delta\boldsymbol{\varphi} \cdot \boldsymbol{F}] : \frac{\partial \boldsymbol{P}^{\mathrm{tot}}}{\partial \boldsymbol{F}} : [\nabla_{\boldsymbol{x}}\Delta\boldsymbol{\varphi} \cdot \boldsymbol{F}] \\ & - J^{-1}[\nabla_{\boldsymbol{x}}\delta\boldsymbol{\varphi} \cdot \boldsymbol{F}] : \frac{\partial \boldsymbol{P}^{\mathrm{tot}}}{\partial \mathbb{E}} \cdot [\nabla_{\boldsymbol{x}}\Delta\boldsymbol{\varphi} \cdot \boldsymbol{F}] \mathrm{dv} \\ & + \int_{\mathcal{B}_t} J^{-1}[\nabla_{\boldsymbol{x}}\delta\boldsymbol{\varphi} \cdot \boldsymbol{F}] \cdot \frac{\partial \mathbb{D}}{\partial \boldsymbol{F}} : [\nabla_{\boldsymbol{x}}\Delta\boldsymbol{\varphi} \cdot \boldsymbol{F}] \\ & - J^{-1}[\nabla_{\boldsymbol{x}}\delta\boldsymbol{\varphi} \cdot \boldsymbol{F}] \cdot \frac{\partial \mathbb{D}}{\partial \mathbb{E}} \cdot [\nabla_{\boldsymbol{x}}\Delta\varphi \cdot \boldsymbol{F}] \,\mathrm{dv}. \end{aligned} \tag{64}$$

In the subsequent derivations we will omit the terms of the Maxwell stress $\boldsymbol{P}^{\max}$ and the free space electric displacement $\mathbb{D}^{\varepsilon}$. Since E_0 is not transferred to the logarithmic strain space, the

contributions of $\boldsymbol{P}^{\max}$ and $\mathbb{D}^{\varepsilon}$ to the variation consist of the standard second order derivatives of E_0. For the remaining terms, a mapping into the logarithmic strain space yields the following expression

$$\begin{aligned}\Delta g^{\mathrm{red}}_{\mathrm{int}}(\boldsymbol{\varphi},\varphi,\delta\boldsymbol{\varphi},\delta\varphi) \;=\; & \int_{\mathcal{B}_t} \nabla_{\boldsymbol{x}}\delta\varphi : \boldsymbol{I}\overline{\otimes}\left[\boldsymbol{\sigma}+\boldsymbol{\sigma}^{\mathrm{pol}}\right] : \nabla_{\boldsymbol{x}}\Delta\varphi \,\mathrm{dv} \\ & + \int_{\mathcal{B}_t} \nabla_{\boldsymbol{x}}\delta\varphi : J^{-1}[\boldsymbol{F}\overline{\otimes}\boldsymbol{F}] : \Big[\mathrm{P}^T : \mathbb{T}_{\boldsymbol{\alpha}} : \mathrm{P} \\ & + [\boldsymbol{S}^{\infty}_{\log}+\boldsymbol{S}^{\nu}_{\log}] : \mathrm{L}\Big] : \left[\boldsymbol{F}^T\overline{\otimes}\boldsymbol{F}^T\right] : \nabla_{\boldsymbol{x}}\Delta\varphi \,\mathrm{dv} \\ & - \int_{\mathcal{B}_t} \nabla_{\boldsymbol{x}}\delta\varphi : J^{-1}[\boldsymbol{F}\overline{\otimes}\boldsymbol{F}] : \left[\mathrm{P}^T : \mathbb{T}_{\boldsymbol{\kappa}}\right]\cdot\boldsymbol{F}^T\cdot\nabla_{\boldsymbol{x}}\Delta\varphi \,\mathrm{dv} \\ & + \int_{\mathcal{B}_t} \nabla_{\boldsymbol{x}}\delta\varphi\cdot J^{-1}\boldsymbol{F}\cdot[\mathbb{T}^T_{\boldsymbol{\kappa}} : \mathrm{P}] : \left[\boldsymbol{F}^T\overline{\otimes}\boldsymbol{F}^T\right] : \nabla_{\boldsymbol{x}}\Delta\varphi \,\mathrm{dv} \\ & - \int_{\mathcal{B}_t} \nabla_{\boldsymbol{x}}\delta\varphi\cdot J^{-1}\boldsymbol{F}\cdot\mathbb{T}_{\boldsymbol{\beta}}\cdot\boldsymbol{F}^T\cdot\nabla_{\boldsymbol{x}}\Delta\varphi \,\mathrm{dv}\end{aligned} \tag{65}$$

with

$$\mathrm{L} \;=\; 4\frac{\partial^2\varepsilon}{\partial\boldsymbol{C}^2}. \tag{66}$$

A detailed definition including algorithms for implementing fourth-order tensor P and the double contraction of the sixth-order tensor L with $[\boldsymbol{S}^{\infty}_{\log}+\boldsymbol{S}^{\nu}_{\log}]$ can be found in Miehe and Lamprecht (2001), Miehe et al. (2002). The geometric tangent in the first row of (65), can be evaluated once we know the corresponding stresses (Reese and Govindjee, 1998). The remaining four integrals form the constitutive tangent, for which an algorithmically consistent derivation is necessary to preserve the quadratic convergence of Newton–Raphson scheme (Simo and Taylor, 1985; ; Wriggers, 2001; Belytschko et al., 2000). Besides the stress tangent $\mathbb{T}_{\boldsymbol{\alpha}}$ (Miehe and Lamprecht, 2001; Miehe et al., 2002),

$$\mathbb{T}_{\boldsymbol{\alpha}} \;=\; \frac{\partial[\boldsymbol{S}^{\infty}_{\log}+\boldsymbol{S}^{\nu}_{\log}]}{\partial\boldsymbol{\varepsilon}} \;=\; \frac{\partial^2\widehat{\psi_0}^{\infty}(\boldsymbol{\varepsilon},\mathbb{E})}{\partial\boldsymbol{\varepsilon}^2} + \mathrm{d}_{\boldsymbol{\varepsilon}}\boldsymbol{S}^{\nu}_{\log}, \tag{67}$$

$$\mathrm{d}_{\boldsymbol{\varepsilon}}\boldsymbol{S}^{\nu}_{\log} := \frac{\partial\boldsymbol{S}^{\nu}_{\log,\mathrm{k+1}}}{\partial\boldsymbol{\varepsilon}_{k+1}} \;=\; E^{4,\nu}(\mathbb{E}_{k+1}) : \left[1^4_{sym} - \mathrm{d}_{\boldsymbol{\varepsilon}}\boldsymbol{\varepsilon}^{\nu}_{k+1}\right], \tag{68}$$

we introduce the electro-mechanical coupling tangent $\mathbb{T}_{\boldsymbol{\kappa}}$

$$\mathbb{T}_{\boldsymbol{\kappa}} \;=\; \frac{\partial[\boldsymbol{S}^{\infty}_{\log}+\boldsymbol{S}^{\nu}_{\log}]}{\partial\mathbb{E}} \;=\; \frac{\partial^2\widehat{\psi_0}^{\infty}(\boldsymbol{\varepsilon},\mathbb{E})}{\partial\mathbb{E}\partial\boldsymbol{\varepsilon}} + \mathrm{d}_{\mathbb{E}}\boldsymbol{S}^{\nu}_{\log}, \tag{69}$$

$$\begin{aligned}\mathrm{d}_{\mathbb{E}}\boldsymbol{S}^{\nu}_{\log} := \frac{\partial\boldsymbol{S}^{\nu}_{\log,\mathrm{k+1}}}{\partial\mathbb{E}_{k+1}} = [\boldsymbol{\varepsilon}_{k+1}-\boldsymbol{\varepsilon}^{\nu}_{k+1}] : \mathrm{d}_{\mathbb{E}}E^{4,\nu}(\mathbb{E}_{k+1}) - E^{4,\nu}(\mathbb{E}_{k+1}) \\ : \mathrm{d}_{\mathbb{E}}\boldsymbol{\varepsilon}^{\nu}_{k+1},\end{aligned} \tag{70}$$

and the purely electrical tangent $\mathbb{T}_{\boldsymbol{\beta}}$ such that:

$$\mathbb{T}_{\boldsymbol{\beta}} \;=\; \frac{\partial[\mathbb{P}^{\infty}+\mathbb{P}^{\nu}]}{\partial\mathbb{E}} \;=\; -\frac{\partial^2\widehat{\psi_0}^{\infty}(\boldsymbol{\varepsilon},\mathbb{E})}{\partial\mathbb{E}^2} + \mathrm{d}_{\mathbb{E}}\mathbb{P}^{\nu}, \tag{71}$$

$$\begin{aligned}\mathrm{d}_{\mathbb{E}}\mathbb{P}^{\nu} := \frac{\partial\mathbb{P}^{\nu}_{k+1}}{\partial\mathbb{E}_{k+1}} \;=\; & [\boldsymbol{\varepsilon}_{k+1}-\boldsymbol{\varepsilon}^{\nu}_{k+1}] \\ & : \mathrm{d}_{\mathbb{E}}E^{4,\nu}(\mathbb{E}_{k+1}) \overset{34}{:} \mathrm{d}_{\mathbb{E}}\boldsymbol{\varepsilon}^{\nu}_{k+1} - \frac{1}{2}[\boldsymbol{\varepsilon}_{k+1}-\boldsymbol{\varepsilon}^{\nu}_{k+1}] \\ & : \mathrm{d}^2_{\mathbb{E}\,\mathbb{E}}E^{4,\nu}(\mathbb{E}_{k+1}) \overset{34}{:} [\boldsymbol{\varepsilon}_{k+1}-\boldsymbol{\varepsilon}^{\nu}_{k+1}].\end{aligned} \tag{72}$$

For our specific choice of the update for the internal variable (58), the algorithmically consistent derivation of the logarithmic strain tensor $\boldsymbol{\varepsilon}^{\nu}_{k+1}$ with respect to $\boldsymbol{\varepsilon}_{k+1}$ results in

$$\mathrm{d}_{\boldsymbol{\varepsilon}}\boldsymbol{\varepsilon}^{\nu}_{k+1} := \frac{\partial\boldsymbol{\varepsilon}^{\nu}_{k+1}}{\partial\boldsymbol{\varepsilon}_{k+1}} \;=\; \frac{\Delta t}{\eta}\mathbb{A}^{-1} : E^{4,\nu}(\mathbb{E}_{k+1}),. \tag{73}$$

With $\mathrm{d}_{\mathbb{E}}\boldsymbol{\varepsilon}_{k+1} = \boldsymbol{0}$, it follows for the derivative with respect to $\mathbb{E}_{k+1}$ that

$$\mathrm{d}_{\mathbb{E}}\boldsymbol{\varepsilon}^{\nu}_{k+1} := \frac{\partial\boldsymbol{\varepsilon}^{\nu}_{k+1}}{\partial\mathbb{E}_{k+1}} \;=\; \frac{\Delta t}{\eta}\mathbb{A}^{-1} : \mathrm{d}_{\mathbb{E}}E^{4,\nu}(\mathbb{E}_{k+1}) \overset{34}{:} [\boldsymbol{\varepsilon}_{k+1}-\boldsymbol{\varepsilon}^{\nu}_{k+1}], \tag{74}$$

where the second double contraction is defined for any fifth order tensor $\boldsymbol{A}$ and fourth order tensor $\boldsymbol{B}$ as $\boldsymbol{A}\overset{34}{:}\boldsymbol{B} = A_{ijklm}B_{klpq}\boldsymbol{e_i}\otimes\boldsymbol{e_j}\otimes\boldsymbol{e_m}\otimes\boldsymbol{e_p}\otimes\boldsymbol{e_q}$. The algorithmic derivatives $\mathrm{d}_{\mathbb{E}}E^{4,\nu}(\mathbb{E}_{k+1})$ and $\mathrm{d}^2_{\mathbb{E}\,\mathbb{E}}E^{4,\nu}(\mathbb{E}_{k+1})$ coincide with the ordinary continuum derivatives $\partial E^{4,\nu}(\mathbb{E})/\partial\mathbb{E}$ and $\partial^2E^{4,\nu}(\mathbb{E})/\partial\mathbb{E}^2$.

5. Numerical results

As prototype for our numerical examples serves a bulk of dielectric elastomer under the stimulation of an electric field. In a real world experiment, two compliant electrodes are adhered to the dielectric material and the applied electric voltage between the electrodes causes a field activated bulk deformation. This movement is useful to set up electro-active materials as actuators of different kind. Although this might not be feasible for all sets of experiments (Begley et al., 2005), we ignore the compliant electrodes within the finite element model due to their negligible thickness in comparison to the polymer film (Pelrine et al., 1998; Begley et al., 2005) and the assumption of perfect adhesion (O'Halloran et al., 2008). All numerical experiments were performed with an in-house finite element code implemented in Fortran90 where the electro-visco-elastic material model has been incorporated. Standard displacement based hexahedral finite elements have been used throughout the simulations.

As a first numerical example, we consider a thin film of dielectric elastomer immersed into an electric field to calibrate the coupling parameters c_1 and c_2. Next, we perform a detailed parametric study of the constants k^{ν}_3, k^{ν}_4, and k^{ν}_5 in the material tensor $E^{4,\mathrm{v}}$ by analyzing the relaxation and hysteresis tests of a thin plate. Both setups resemble an extending actuator. Finally, we study a bimorph bending actuator where we put special emphasis to the large deformations of the structure and the creep behavior due to viscosity. We restrict ourselves to an investigation containing a single Maxwell element. Table 1 summarizes the set of material parameters, from which the mechanical parameters in E^4 and $E^{4,\mathrm{v}}$ can be calculated as $k^e_1 = k^{\nu}_1 = \kappa - \frac{2}{3}\mu$ and $k^e_2 = k^{\nu}_2 = \mu$. For the quasi-static simulations, the elapsed time between two load steps is $\Delta t = 1$ s. Dielectric elastomeric films have been investigated in a thickness range from several micro- to millimeter (Pelrine et al., 1998; Brochu and Pei, 2010; O'Halloran et al., 2008). We will present our numerical examples in the micrometer regime. However, a multiplication by the factor 10^3 of the applied actuation voltage, the geometric dimensions and the resulting displacement translate the results to the millimeter regime.

5.1. Thin film immersed in an electric field (extending actuator)

First, we consider a thin film with dimensions 5 μm × 5 μm × 1.25 μm, discretized by 8 × 8 × 8 hexahedral elements. Electrodes fully cover its top and bottom (See Fig. 3a). We apply homogeneous Dirichlet boundary condition at the bottom corner at (−2.5 μm, −2.5 μm, −0.625 μm), while the material is free

Table 1
The material parameter are chosen with regard to silicones or acrylic elastomers (e.g. VHB 4910 by 3M) as an example of a soft dielectric elastomers with distinct electrostrictive behavior and low electric permittivities.

Parameter	Unit	Value	Reference
μ	MPa	0.0473	Experimentally derived in Wissler and Mazza (2007)
κ	MPa	2.349	Results from ν=0.49, within range of Pelrine et al. (1998); Brochu and Pei (2010)
η	MPas	1	Used in Büschel et al. (2013), same order as in Khan et al. (2013)
ε_0	N/V^2	$8.85\cdot10^{-12}$	(Jackson, 1999)
c_1	N/V^2	-10^{-10}	Relative permittivity of 10^0 as in Pelrine et al. (1998); Kofod et al. (2001); Wissler and Mazza (2007); Brochu and Pei (2010)
c_2	N/V^2	10^{-10}	High strains (Bar-Cohen, 2002; Bar-Cohen, 2004; Pelrine et al., 2000b; Kofod et al., 2001; O'Halloran et al., 2008) below breakdown field[a]

[a] The break-down electric field depends heavily on prestraining the material or not. Depending on the prestrain of the material, the electric breakdown strength varies in the range of 18 MV/m–218 MV/m for VHB 4910 in Kofod et al. (2001) and within 50 MV/m–200 MV/m for silicones in (Pelrine et al. 1998). According to (Brochu and Pei 2010) the maximal possible fields for unprestrained materials are around 72–235 MV/m for silicones, at 8–160 MV/m for polyurethanes, and within 17–34 MV/m for VHB 4910. Prestraining can lead to a breakdown field of up to 350 MV/m for silicones and up to 412 MV/m for VHB 4910.

to expand in the x-y plane and to contract in z direction. The compliant electrodes are loaded with an electric voltage of −0.5 V on top and +0.5 V on bottom per load step until an electromechanical instability (Plante and Dubowsky, 2006; Khan et al., 2013) occurs at a total potential difference of 37 V. In this example, we neglected viscous effects.

Fig. 3b visualizes a comparison of the undeformed and deformed configuration. The resulting deformation and electric field strength are homogeneous throughout the bulk. The maximal contraction within the direction of the electric field is about 70%, while an area strain of 82% can be observed. Due to this pronounced enlargement in the x–y plane, dielectric elastomers serve well as extending actuators. At the highest strain level, the electric field strength does not exceed 100 MV/m, which lies within a representative range of actuation fields. The approximate relative permittivity varies between the order of $10^1 \ldots 10^0$. Fig. 4 clearly visualizes the influence of the electric free field energy at low dielectric constants. The contraction reaches only 60% of the maximal value when we ignore the free field energy E_0 within the simulation.

5.2. Thin plate under electric and mechanical loading in parallel

For the parametric study of the electro-visco-elastic material model we investigate at first a thin plate under electric and mechanical loading, such that the direction of the electrical field and the tensile direction coincide. Fig. 5a shows the plate (120 μm × 40 μm × 5 μm) and the boundary conditions. Two electrodes are located at the front faces of the plate. At $X = 0$ μm, the electrode and the dielectric are completely fixed, while the electrode at $X = 120$ μm can move with the film in longitudinal (x) direction. However, floating bearings $X = 120$ μm prohibit a change in area of the compliant electrode and at the front face of the elastomer. Fig. 5b depicts a contour plot of the actuation voltage applied to the structure discretized by 24 × 8 × 4 hexahedral elements.

What follows is a detailed analysis of the electro-visco-elastic model by separately increasing the six electro-mechanical coupling parameters in the structural tensors E^4 and $E^{4,v}$ throughout a series of relaxation tests. For selected values, we perform hysteresis simulations to show the energy dissipating character of the viscous material model.

5.2.1. Relaxation test on thin plate (parallel)

For the relaxation test, we stretch the film about 25% of its original length in longitudinal (x) direction within 5 load steps. The resulting strain rate of $\dot{\lambda}_x = 0.05$ s mimics an instant stretch of the structure. At the same time, we increase the electric voltage up to $2.7\cdot10^3$ V at the electrode at $X = 120$ μm. This results in the mid point $\boldsymbol{X}_{\text{mid}} = (60\ \mu\text{m} \times 20\ \mu\text{m} \times 2.5\ \mu\text{m})$ of the film in an one-dimensional electric field $e_x = 18$ MV/m. After the loading procedure, we keep the film at the stretched position for 100 load steps to observe the relaxation of the stress in tensile direction.

Fig. 6 shows the deformed structure right after the loading procedure (a) and after the phase of relaxation (b). The color code represents the tensile stress $\boldsymbol{\sigma}^{\text{tot}}_{xx}$. As typical for visco-elastic materials, the stress inside the material declines to a certain threshold during the relaxation interval. Due to the inhomogeneous deformation, we analyze the stress response in a single point $\boldsymbol{X}_{\text{mid}}$ at the center of the plate, where the stress and the strain state is almost homogeneous.

Fig. 7 documents the significant influence of the coupling parameters k^3_ν through k^5_ν on the relaxation curves. The exponential

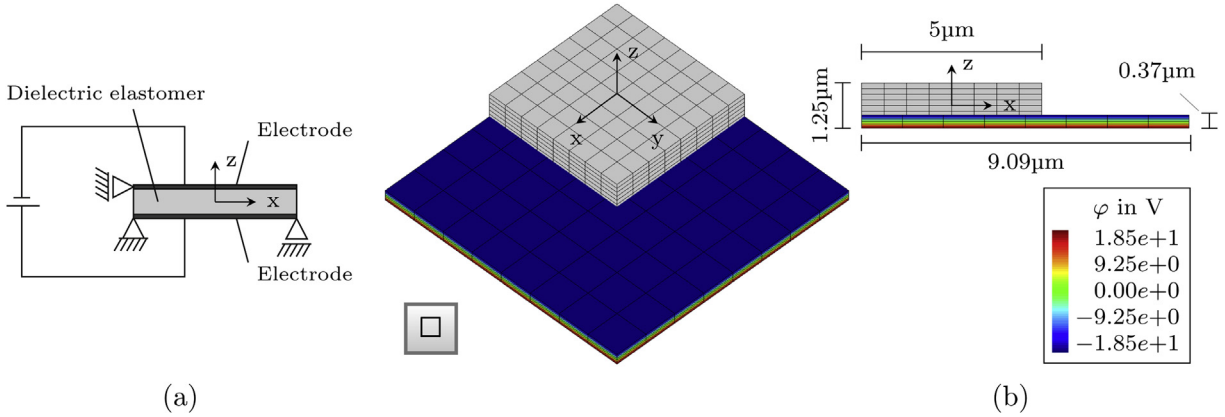

Fig. 3. Thin film under electric voltage: (a) Geometric setup and applied boundary conditions; (b) Comparison of undeformed and resulting deformed configuration in isometric view and in x–z plane.

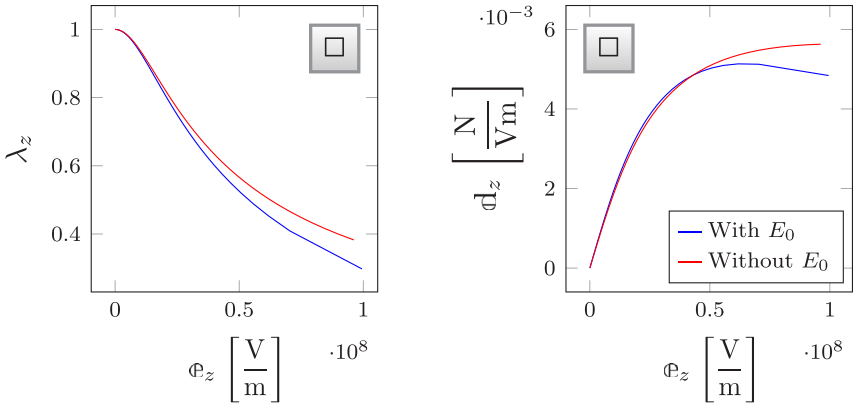

Fig. 4. Thin film under electric voltage from $\Delta\varphi = 0$ V to $\Delta\varphi = 37$ V: Plot of evolution of stretch λ_z and electric displacement $\mathbb{d}_z$ over electric field $\mathbb{e}_z$ with and without consideration of the free field electric energy E_0.

decrease in tensile stress illustrates the viscous material response. The curves show that the material reaches a completely relaxed state already after 50 steps of relaxation. Furthermore, the total stress response is higher as soon as an electric field is applied. This is due to the compliant electrodes, which tend to attract each other and thus exert a ponderomotive stress on the bulk. This compressive stress hinders the stretching of the material. Fig. 7a shows that an increase in k_ν^3 leads to a relaxation process already during the loading phase. For high values of k_ν^3, the material is at a relaxed state by the time the loading path is completed. Thus, the material behaves more and more elastic or in other words, an increase of k_ν^3 leads to a decrease in the corresponding viscosity parameter. Fig. 7b and c illustrate that, in contrast to Fig. 7a, increasing the values of k_ν^4 and k_ν^5 yields an overall stiffer material response and a decrease in relaxation time. Relaxation takes place at a much faster rate as in the experiments when k_ν^4 and k_ν^5 were set to zero.

5.2.2. Hysteresis test on thin plate (parallel)

For the hysteresis tests, we first stretch the material about 25% of its original length followed by a compression via the neutral position until the structure has shortened in longitudinal direction about 25% of its original length. Fig. 8 illustrates the fully elongated (a), compressed (b) and neutral position (c). We repeat this loop three times to reach the steady state and perform it at two different strain rates of $\dot{\lambda}_x = 0.01\ \mathrm{s}^{-1}$ and $\dot{\lambda}_x = 0.02\ \mathrm{s}^{-1}$. Thus, one hysteresis loop consists of 100 or 50 increments corresponding to 100 or 50 s. The simulation closes with 100 relaxation steps, during which the structure recovers its initial configuration.

Within the very first 5 load steps, we apply two different actuation voltages of $5.4 \cdot 10^2$ V and $1.08 \cdot 10^3$ V, which equals a total potential difference of $\Delta\varphi = 2.7 \cdot 10^3 \Delta\phi = 2.7 \cdot 10^3$ V and $5.4 \cdot 10^3$ V. At full elongation, this results in the mid point $\boldsymbol{X}_{\mathrm{mid}}$ of the film in an one-dimensional electric field of $\mathbb{e}_x = 18$ MV/m and $\mathbb{e}_x = 36$ MV/m.

Fig. 9 summarizes the evolution of the longitudinal stress $\boldsymbol{\sigma}_{xx}^{\mathrm{tot}}$ over stretch λ_x for diverse loadings and material parameters. We conclude that the stronger the applied electric field, the higher the hysteresis curve is shifted translationally upwards along the y-axis. When no electric field is applied, the curve circles symmetrically around the origin with equally distributed periods of pull and compression. However, under the influence of an electric field, which leads to a contraction of the material in x-direction, the phase of pull prevails. For even higher fields, the hysteresis curve lies completely in the positive stress range. Independent of the strength of the electric field, the inclination of the hysteresis curve increases for higher strain rates because at faster loading procedures less relaxation takes places during the elongation of the plate. As a consequence, the maximum value of the longitudinal stress can be significantly higher.

Fig. 9b–d document the effects of alternating the viscous coupling parameters k_3^ν through k_5^ν during the hysteresis experiments. The results are well in line with the relaxation tests. Since increasing of k_ν^3 leads to a relaxation process already during the loading phase, the material behaves more and more elastic. Fig. 9b shows a decrease in area enclosed by the hystereses as k_ν^3 increases. This is contrary to the observed changes in Fig. 9c and d, when

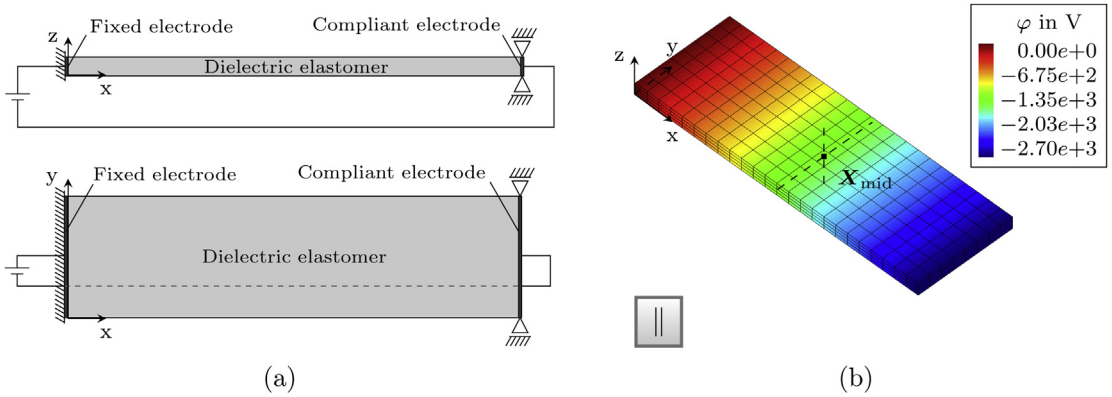

Fig. 5. Thin plate (120 μm × 40 μm × 5 μm) under electric voltage such that electric field is directed parallel to the mechanical loading: (a) Geometric setup and applied boundary conditions; (b) Electric potential on discretized plate.

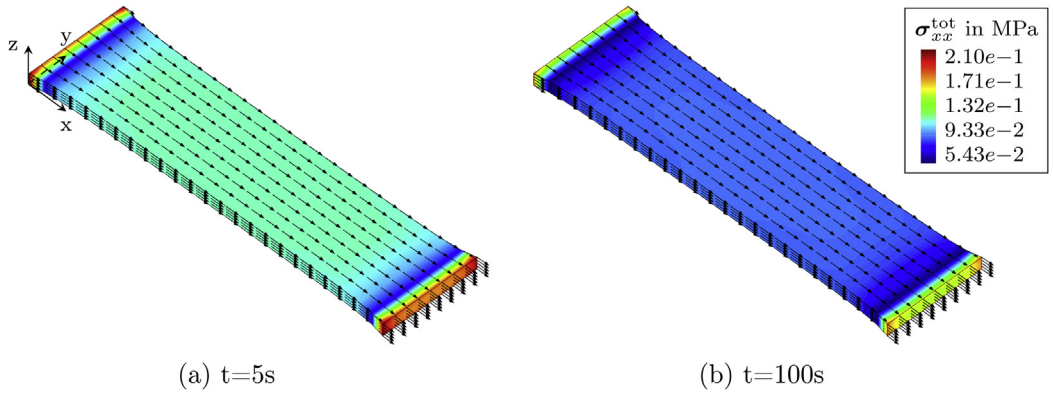

Fig. 6. Relaxation test on thin plate under electric voltage such that electric field is directed parallel to the mechanical loading: Contour plot of total stress σ^{tot}_{xx} and vector plot of $\mathbb{e}_x$ during relaxation test right after loading procedure (a) and at relaxed state (b).

setting k_v^4 and k_v^5 to higher values. Higher values of k_v^4 and k_v^5 result in a widening of the curve, corresponding to an increase in energy dissipation.

5.3. Thin plate under electric stimulation perpendicular to mechanical loading

The second part of the parametric study deals with a thin plate under electric and mechanical loading, where in comparison to Section 5.2, the position of the compliant electrodes has shifted. As depicted in Fig. 10a, the electrodes are now located at the top and bottom sides of the plate at $z = 5$ µm and $z = 0$ µm. Both compliant electrodes are able to stretch within the x–y plane. Additionally, they follow the deformation of the elastomer, which further increases the electric field inside the material. We select an electric loading that mimics the electric field strength of Section 5.2. Therefore, we apply stepwise an electric loading of −7.5 V on the top and 7.5 V on the bottom electrode, which results in a total potential difference of $\Delta\varphi = 75$ V after 5 load steps. Fig. 10b depicts a contour plot of the actuation voltage. In the mid point $\boldsymbol{X}_{\text{mid}}$ of the film in fully stretched state, this leads to an electric field in z-direction of $\mathbb{e}_z \approx 18.55$ MV/m. For the relaxation and hysteresis tests, the same mechanical loading is applied as described in Section 5.2. We perform five hysteresis loops to reach the steady state.

5.3.1. Relaxation test on thin plate (perpendicular)

The relaxation test results in Fig. 11 differ from those in Section 5.2.1 in two ways: The first and obvious difference is the lower stress response at the electrically activated state (—) in comparison to the purely mechanical case (- -). The compliant electrodes tend to contract in z-direction, which causes the material to elongate in the orthogonal x–y plane. Thus, the force necessary to pull the material to a certain prescribed displacement is less under the stimulation by an electric field than without. A strong increase in the viscous coupling parameter k_4^v and k_5^v annihilates this effect. This does not apply for an increase in k_3^v, since here the rapid relaxation overweights yet during the loading procedure. The second difference is that only the viscous coupling parameters produce a significant change in the relaxation curves, which are at least one order of magnitude higher than those on Section 5.2.1.

5.3.2. Hysteresis tests on thin plate (perpendicular)

Fig. 12 shows a collection of hysteresis graphs for the perpendicular case. In agreement with Fig. 11, hysteresis curves for tests with an electric field lie below those without an electric field. A bigger part of the ellipses shifts into the negative tensile stress range. Thus, compression dominates the hysteresis and leads to a structural instabilities. In the simulations, we observe buckling associated with problems of algorithmic convergence. To avoid a loss of convergence due to buckling, we restrain the x-y plane of the

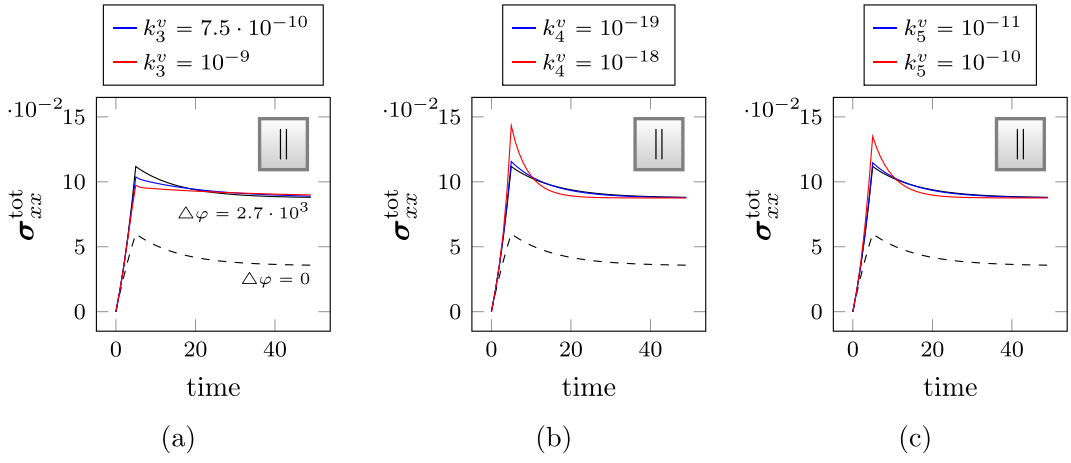

Fig. 7. Relaxation test on thin plate under electric voltage such that electric field is directed parallel to the mechanical loading: Influence of variation of k_3^v [N/V^2], k_4^v [Nmm^2/V^4], and k_5^v [N/V^2] on the longitudinal stress σ^{tot}_{xx} [MPa] over time [s]. The dashed black graph denotes the purely mechanical reference case, while the solid black graph denotes the electro-mechanical reference case for $k_3^v, k_4^v, k_5^v = 0$.

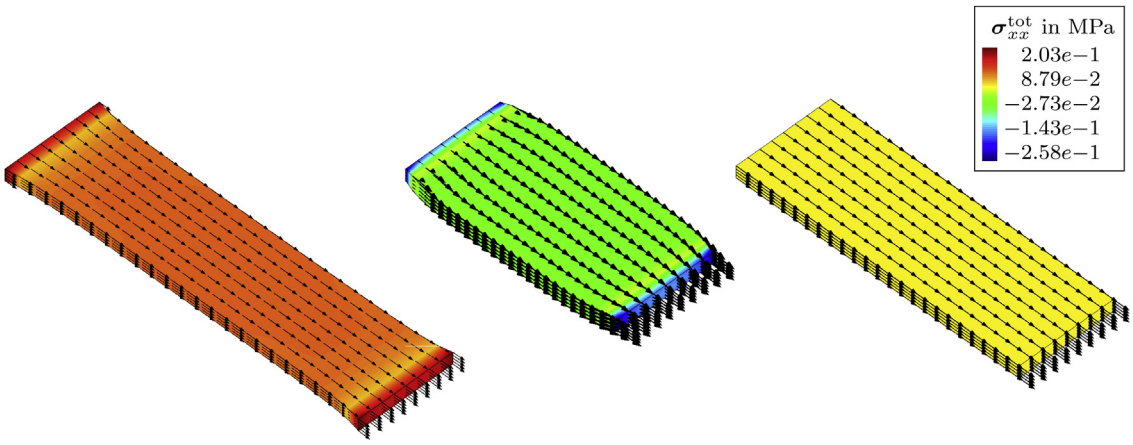

Fig. 8. Thin plate under electric voltage such that electric field is directed parallel to the mechanical loading: Contour plot of total stress $\boldsymbol{\sigma}^{\text{tot}}_{xx}$ and vector plot of $\mathbb{e}_x$ during hysteresis test at full extension (a), contraction (b) and in relaxed neutral position (c).

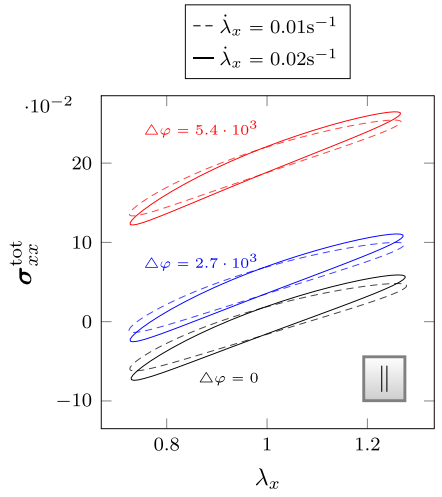

(a) Comparison of different strain rates and electric loading ramps for $k_3^v = k_4^v = k_5^v = 0$

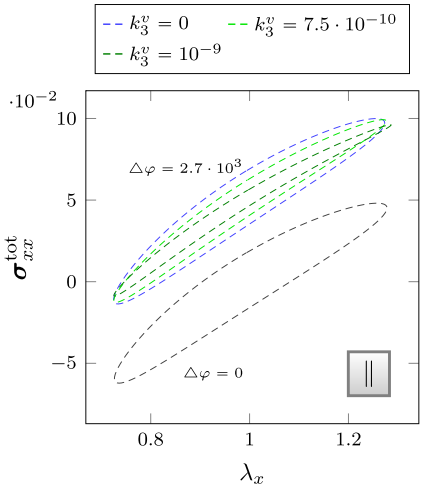

(b) $\dot{\lambda}_x = 0.01\text{s}^{-1}$. For a comparison with (a) note the different scaling of vertical axis.

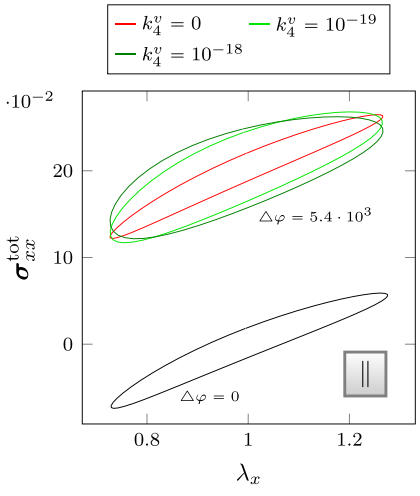

(c) $\dot{\lambda}_x = 0.02\text{s}^{-1}$

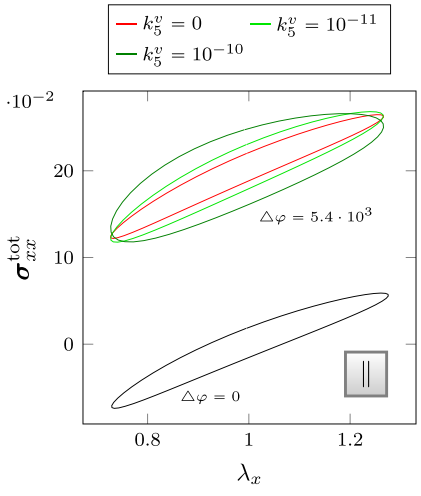

(d) $\dot{\lambda}_x = 0.02\text{s}^{-1}$

Fig. 9. Hysteresis test on thin plate under electric voltage such that electric field is directed parallel to the mechanical loading: Influence of variation of electric voltage, strain rate and of coupling parameter k_3^v [N/V^2], k_4^v [Nmm^2/V^4], and k_5^v [N/V^2] on the longitudinal stress $\boldsymbol{\sigma}^{\text{tot}}_{xx}$ [MPa] over strain. The black graphs denote the purely mechanical reference case.

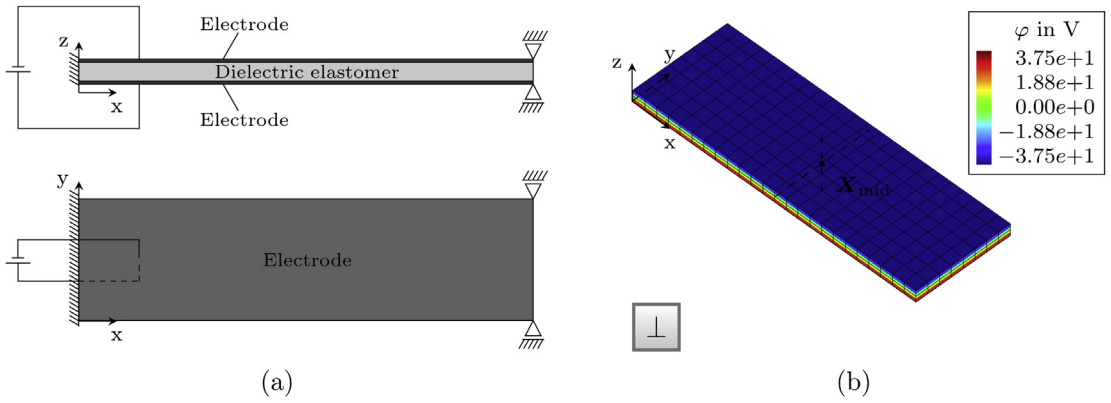

Fig. 10. Thin plate (120 μm × 40 μm × 5 μm) under electric voltage such that electric field is directed perpendicular to the mechanical loading: (a) Geometric setup and applied boundary conditions; (b) Electric potential on discretized plate.

plate at $z = 2.5$ μm in z direction. With this modification in the boundary conditions we complete the study and document the results in Fig. 12. An increase in k_3^v leads to a thinning of the hysteresis curve, whereas an increase in k_4^v and k_5^v leads to a widening of the hysteresis curve.

5.4. Thin film composite material under electric field

5.4.1. Bimorph bending actuator

As a next example, we consider a bimorph bending actuator of a bi-layered thin film. Fig. 13a shows a sketch of the composite material. The structure has the same dimensions and discretization as the plate studied in Sections 5.2 and 5.3. The bottom layer of the dielectric elastomer is sandwiched between a pair of compliant electrodes located at the composite's bottom at $z = 0$ μm and in the mid plane at z =2.5 μm. The upper layer consists of an ordinary visco-elastic material that is electrically passive. The bearing of the composite film is designed with the objective to render the largest possible bending deformation. The structure is fixed at $X = Z = 0$, but free to move in z direction throughout. Motion is restrained in y direction along the longitudinal boundaries of the actuator. The electric field is directed through the thickness of the active layer, which causes it to contract. Because of the bearings along the longitudinal sides of the elastomer, any compression in z direction is redirected into the largest possible deformation of the active layer in x direction. Since the active layer is perfectly adhered to the passive layer, the structure gradually bends towards the active layer.

Fig. 14a demonstrates the role up of the structure for distinct time steps. We activate the composite by an electric voltage of −50 V evenly distributed in space and time within 100 load steps. For the moment, we neglect viscous effects. The loading results inside the dielectric layer in a maximal electric field magnitude of $\|\mathbb{e}\| = 23.7$ MV/m. Throughout the curling up of the structure, the electric field is homogeneous and always directed through the thickness direction. Fig. 15a visualizes the evolution of the magnitude and direction of the electric field with increasing bending deformation at the tip of plate $\boldsymbol{X}_{\text{tip}}$. The tip, originally located at (120 μm, 0 μm, 1.25 μm), covers a distance of 151.3 μm to reach its final position at (−29 μm, 0 μm, 24.9 μm).

In a second simulation, we show the influence of viscosity for $k_4^v = 10^{-18}$ Nmm^2/V. We increase the electric loading from 0 V to −25 V within 50 load steps and keep this level for another 100 time steps. Although kept at constant loading, the structure continues to move and bend. Responsible for the creep is the constant ponderomotive stress exerted through the electrodes on the active layer in combination with the visco-elastic material model. During the loading period, the tip of the plate covers a distance of 50.8 μm. At the end of the observed period of creep, the point has covered in total of

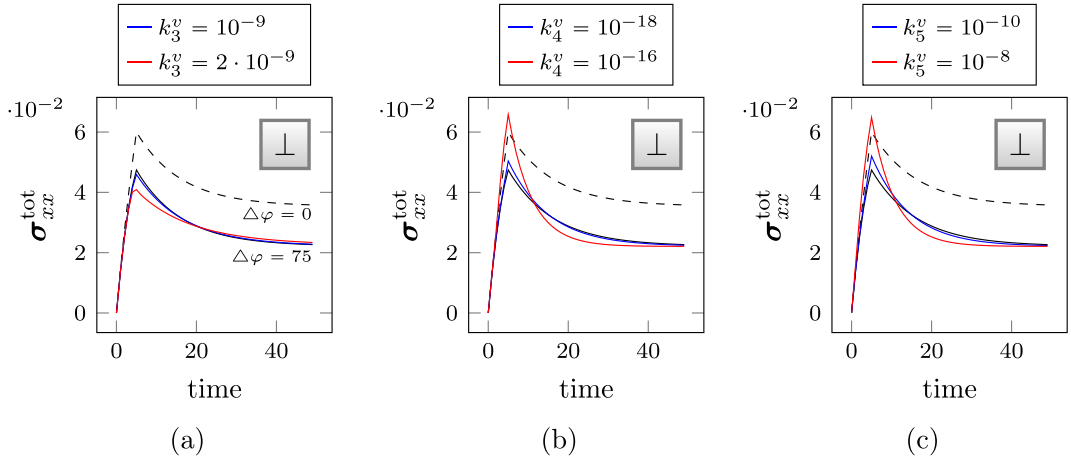

Fig. 11. Relaxation test on thin plate under electric voltage such that electric field is directed perpendicular to the mechanical loading: Influence of variation of k_3^v [N/V^2], k_4^v [Nmm^2/V^4], and k_5^v [N/V^2] on the longitudinal stress $\boldsymbol{\sigma}_{xx}^{\text{tot}}$ over time [s]. The dashed black graph denotes the purely mechanical reference case, while the solid black graph denotes the electro-mechanical reference case for $k_3^v, k_4^v, k_5^v = 0$.

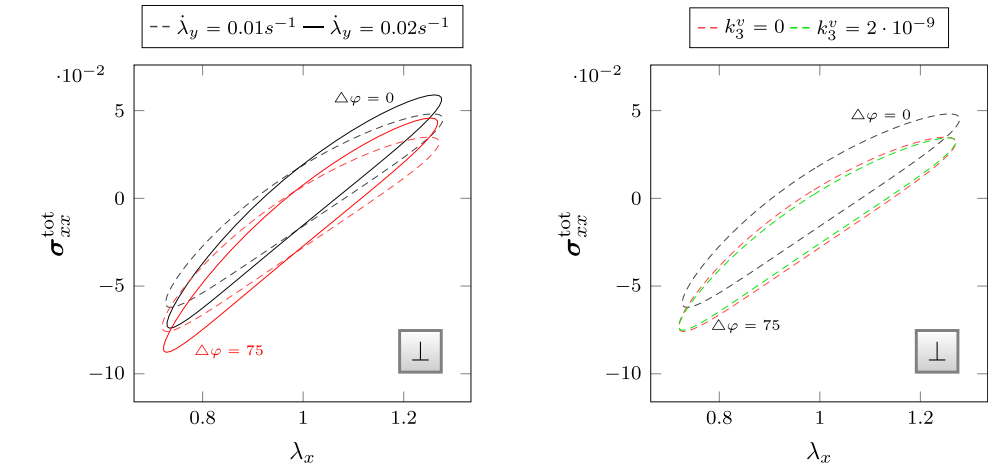

(a) Comparison of different strain rates ramps for $k_3^v = k_4^v = k_5^v = 0$

(b) $\dot{\lambda}_x = 0.01\text{s}^{-1}$

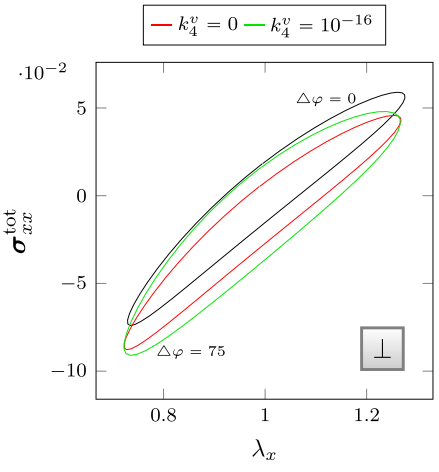

(c) $\dot{\lambda}_x = 0.02\text{s}^{-1}$

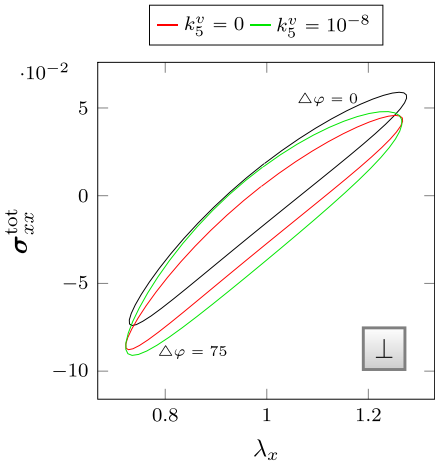

(d) $\dot{\lambda}_x = 0.02\text{s}^{-1}$

Fig. 12. Hysteresis test on thin plate under electric voltage of $\Delta\varphi = 75$ V such that electric field is directed perpendicular to the mechanical loading: Influence of variation of strain rate and of coupling parameter k_3^v [N/V^2], k_4^v [Nmm^2/V^4], and k_5^v [N/V^2] on the longitudinal stress $\boldsymbol{\sigma}^{\text{tot}}_{xx}$ [MPa] over strain. The black graphs denote the purely mechanical reference case.

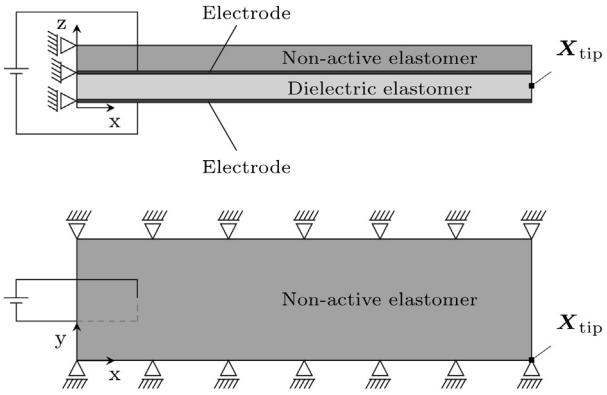

(a)

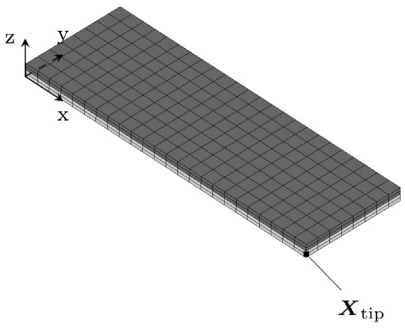

(b)

Fig. 13. Bending actuator under electric voltage such that electric field is directed in thickness direction: (a) Geometric setup and applied boundary conditions; (b) discretized composite plate.

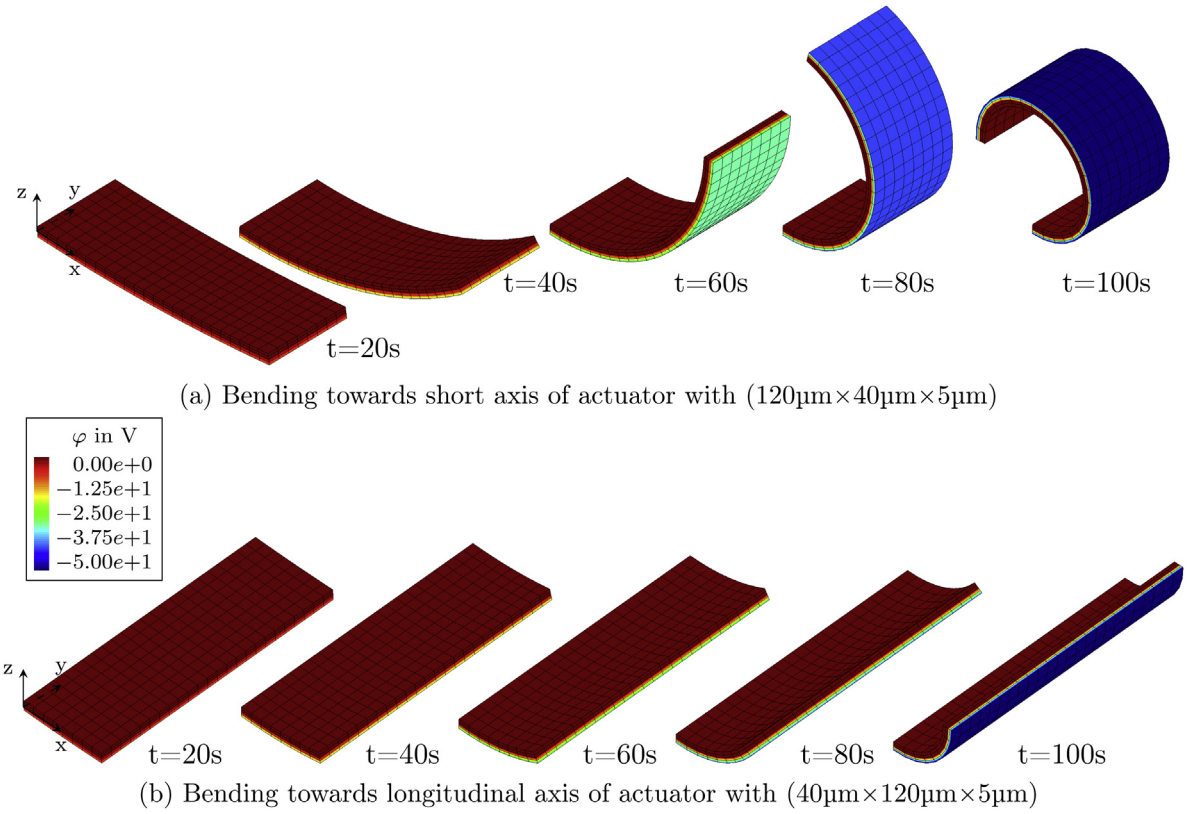

Fig. 14. Bending actuator under electric voltage such that electric field is directed in thickness direction: Deformation due to applied voltage.

62.6 µm. Overall, the mechanism of creep causes additional deformation of about 23%, which might be crucial in the design of real world actuators.

In a third simulation, we rotate the actuator about 90 degrees around the positive z-axis such that the x- and y-dimensions of the plate flip around to (40 µm, 120 µm, 5 µm). $\boldsymbol{X}_{\text{tip}}$ is now located at (40 µm, 0 µm, 1.25 µm). We repeat the electrical loading as before and observe a bending towards the longitudinal side of the actuator. Fig. 14b illustrates the gradual deformation of the flat plate towards a tube. An additional bending of about 17% takes place during the relaxation period, which has to be considered for the layout of a technical device.

5.4.2. *Diaphragm actuator*

For our final example, we modify the mechanical boundary condition of the bending actuator in Section 5.4.1 such that a

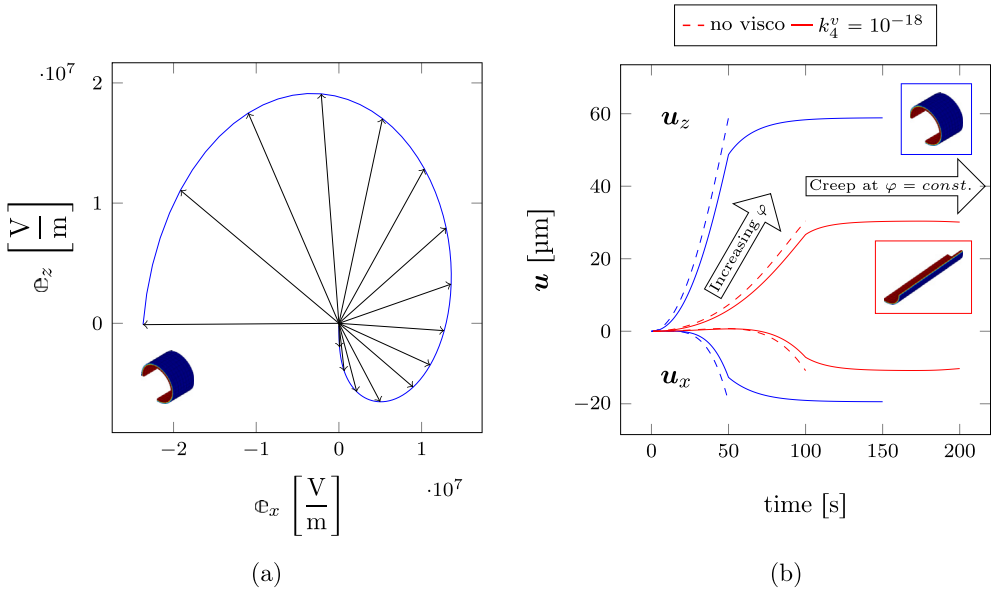

Fig. 15. Bending actuator under electric voltage such that electric field is directed in thickness direction: (a) Evolution of electric field with time and (b) influence of viscosity on deformation observed at $\boldsymbol{X}_{\text{tip}}$.

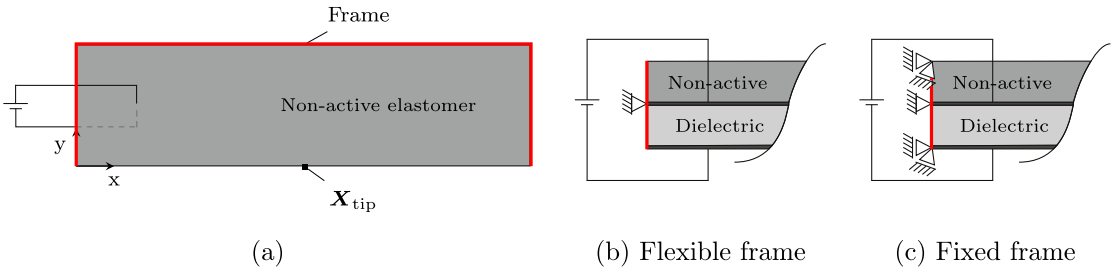

Fig. 16. Diaphragm actuator under electric voltage such that electric field is directed in thickness direction: (a) Geometric setup and applied boundary conditions along red line: (b) flexible frame and (c) fixed frame. (For interpretation of the references to color in this figure legend, the reader is referred to the web version of this article.).

variant of a diaphragm actuator evolves. Fig. 16a shows the three-sided frame, which holds the structure in place. We prescribe two different boundary conditions along the frame. In a first simulation, we fix the circumferential common line of the active and passive layer along the frame, but allow a tilting of the sides around the joint line as in Fig. 16b. In a second simulation, we additionally fix the degrees of freedom within the frame above and below the common line in x and y direction (Fig. 16c). Thus, only an elongation or contraction in thickness direction is possible at framed boundary sides of the elastomer. We apply the electric loading of 50 V within 100 steps and keep it at this level for another 100 steps.

Fig. 17 illustrates the different results in deformation for the two types of boundary conditions. Depending on the imposed constraints in deformation, the electric stimulation causes either a downward inflation of the structure for the flexible frame or an upward gaping for the fixed frame. Both outcomes give inspirations for numerous applications in technical devices. For the case of a flexible frame, the deformation reminds of loudspeakers or excitation devices in shakers, an operation area typically occupied by piezoelectric material. For the fixed frame, a second bi-layered film arranged in mirror pattern should complement the structure to serve in future devices as opening and closing mechanism in the style of a human mouth or vocal cords.

The graphs in Fig. 18 demonstrate that the influence of creep due to the viscous material model is significant on the final deformation. An increase in the viscous parameter k_4^v leads not only to a smoothing of the transition from loading to relaxation phase, but also has a stabilizing effect in the deformation. For a structure clamped to the flexible frame, an increase in k_4^v avoids buckling during the loading phase and retards this trend during the relaxation phase.

6. Conclusion

The design of functional electro-active materials is a major challenge in material sciences. Their behavior are typically highly

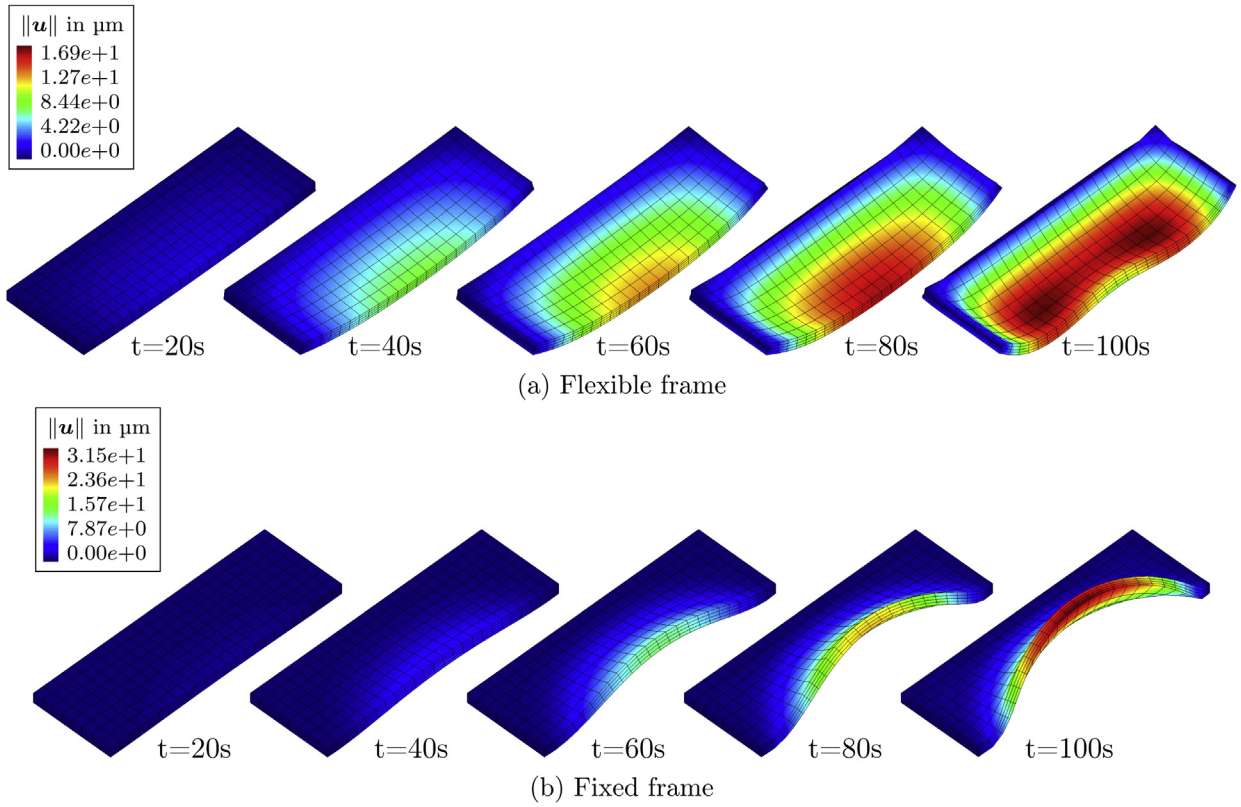

Fig. 17. Diaphragm actuator under electric voltage such that electric field is directed in thickness direction: Bending deformation due to applied voltage for different boundary conditions.

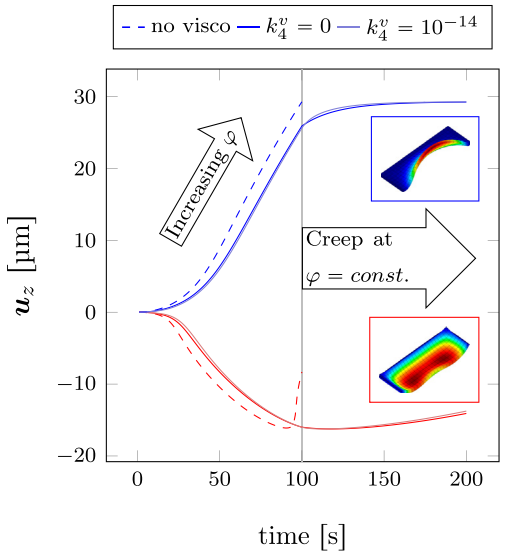

Fig. 18. Diaphragm actuator under electric voltage such that electric field is directed in thickness direction: Evolution of deformation and influence of viscosity observed at $\boldsymbol{X}_{\text{tip}}$.

non-linear both geometrically and constitutively. Mathematical models and computer simulations can help to increase our understanding of electro-active materials and to improve the design of electro-active structures. Here, we have derived a general framework to model and simulate viscous electro-active materials at finite deformations and finite strains. To demonstrate the features of our viscous electro-active model, we have performed systematic parameter sensitivity analyses. With these results, we have illustrated the design of different electro-active actuators and predicted their response when immersed in an electrical field. The advantage of the use of logarithmic strains when incorporating visco- or plastoelastic material models, should not mask the fact that the above defined free energy function does not meet the ellipticity requirements for very large strains. This should be considered when applying the developed model for real life actuator geometries. We believe that our algorithm could serve as a valuable design tool for smart actuators in micro-electro-mechanical systems, microfluidic devices, in robotics, such as artificial skin, tactile displays, artificial muscle, or stimuli-responsive gels.

Acknowledgments

The first author is grateful to the German Research Foundation (Deutsche Forschungsgemeinschaft, DFG) for the funding this work with Grant STE 544/32-2. The financial support of the European Research Council (ERC) with the ERC Advanced Grant 289049 is gratefully acknowledged by the third author. The fourth author would like to express her gratitude to the National Science Foundation through the CAREER award CMMI 0952021 and to the National Institutes of Health through the grant U54 GM072970.

References

Ask, A., Menzel, A., Ristinmaa, M., 2012a. Electrostriction in electro-viscoelastic polymers. Mech. Mater. 50, 9–21.
Ask, A., Menzel, A., Ristinmaa, M., 2012b. Phenomenological modeling of viscous electrostrictive polymers. Int. J. Nonlinear Mech. 47 (2), 156–165.
Bar-Cohen, Y., 2004. Electroactive Polymer (EAP) Actuators as Artificial Muscles. SPIE Press, Bellingham.
Bar-Cohen, Y., 2002. Electro-active polymers: current capabilities and challenges. Proc. SPIE 4695, 1–7.
Begley, M., Bart-Smith, H., Scott, O., Jones, M., Reed, M., 2005. The electro-mechanical response of elastomer membranes coated with ultra-thin metal electrodes. J. Mech. Phys. Solids 53 (11), 2557–2578.
Belytschko, T., Liu, W., Moran, B., 2000. Nonlinear Finite Elements for Continua and Structures. John Wiley & Sons Ltd.
Brochu, P., Pei, Q., 2010. Advances in dielectric elastomers for actuators and artificial muscles. Macromol. Rapid Commun. 31 (1), 10–36.
Büschel, A., Klinkel, S., Wagner, W., 2013. Dielectric elastomers – numerical modeling of nonlinear visco-electroelasticity. Int. J. Numer. Methods Eng., 834–856.
Bustamante, R., Dorfmann, L., Ogden, R.W., 2009. Nonlinear electroelastostatics: a variational framework. Z. Angew. Math. Phys. 60 (1), 154–177.
Bustamante, R., 2009. A variational formulation for a boundary value problem considering an electro-sensitive elastomer interacting with two bodies. Mech. Res. Commun. 36 (7), 791–795.
Chen, X., 2010. Nonlinear electro-thermo-viscoelasticity. Acta Mech. 211 (1–2), 49–59.
Dorfmann, L., Ogden, R.W., 2003. Magnetoelastic modeling of elastomers. Eur. J. Mech. A. Solids 22, 497–507.
Dorfmann, L., Ogden, R.W., 2006. Nonlinear electroelastic deformations. J. Elast. 82 (2), 99–127.
Dorfmann, L., Ogden, R.W., 2005. Nonlinear electroelasticity. Acta Mech. 174 (3–4), 167–183.
El Sayed, T., Mota, A., Fraternali, F., Ortiz, M., 2008. A variational constitutive model for soft biological tissues. J. Biomech. 41 (7), 1458–1466.
Ericksen, J.L., 2007. Theory of elastic dielectrics revisited. Arch. Ration. Mech. Anal. 183 (2), 299–313.
Eringen, A.C., 1963. On the foundations of electroelastostatics. Int. J. Eng. Sci. 1 (1), 127–153.
Fosdick, R., Tang, H., 2007. Electrodynamics and thermomechanics of material bodies. J. Elast. 88 (3), 255–297.
Germain, S., Scherer, M., Steinmann, P., 2010. On inverse form finding for anisotropic hyperelasticity in logarithmic strain space. Int. J. Struc. Changes Solids 2 (2), 1–16.
Holzapfel, G., 2001. Nonlinear Solid Mechanics. Chichester: John Wiley & Sons Ltd.
Hossain, M., Vu, D.K., Steinmann, P., 2012. Experimental study and numerical modelling of VHB 4910 polymer. Comput. Mater. Sci. 59, 65–74.
Jackson, J.D., 1999. Classical Electrodynamics, vol. 3. Wiley.
Johlitz, M., Steeb, H., Diebels, S., Chatzouridou, A., Batal, J., Possart, W., 2007. Experimental and theoretical investigation of nonlinear viscoelastic polyurethane systems. J. Mater. Sci. 42 (23), 9894–9904.
Khan, K.A., Wafai, H., Sayed, T.E., 2013. A variational constitutive framework for the nonlinear viscoelastic response of a dielectric elastomer. Comput. Mech. 52 (2), 345–360.
Kofod, G., Kornbluh, R., Pelrine, R., Sommer-Larsen, P., Bar-Cohen, Y., 2001. Actuation response of polyacrylate dielectric elastomers. Proc. SPIE 4329, 141–147.
Lax, M., Nelson, D.F., 1971. Linear and nonlinear electrodynamics in elastic anisotropic dielectrics. Phys. Rev. B 4 (10), 3694–3731.
Liu, I.-S., 2002. Continuum Mechanics. Springer.
Maugin, G.A., 2009. "On modelling electromagnetomechanical interactions in deformable solids. Int. J. Adv. Eng. Sci. Appl. Math. 1 (1), 25–32.
Maugin, G.A., 1977. On the equations of the electrodynamics of deformable bodies of finite extent. J. Mec. 16 (1), 101–147.
Maugin, G.A., Eringen, A.C., 1990. Electrodynamics of Continua. Springer, Berlin.
Mazzoldi, A., Carpi, F., Rossi, D.d., 2004. Polymers responding to electrical or electrochemical stimuli for linear actuators. Ann. Chim. Sci. Mater. 29 (6), 55–64.
McMeeking, R.M., Landis, C.M., Jimenez, S.M.A., 2007. A principle of virtual work for combined electrostatic and mechanical loading of materials. Int. J. Nonlinear Mech. 42 (6), 831–838.
Miehe, C., Göktepe, S., Méndez Diez, J., 2009. Finite viscoplasticity of amorphous glassy polymers in the logarithmic strain space. Int. J. Solids Struct. 46 (1), 181–202.
Miehe, C., Apel, N., Lamprecht, M., 2002. Anisotropic additive plasticity in the logarithmic strain space: modular kinematic formulation and implementation based on incremental minimization principles for standard materials. Comput. Methods Appl. Mech. Eng. 191, 5383–5425.
Miehe, C., Lamprecht, M., 2001. Algorithms for computation of stresses and elasticity moduli in terms of Seth-Hill's family of generalized strain tensors. Commun. Numer. Methods Eng. 17, 337–353.
Miehe, C., Méndez Diez, J., Göktepe, S., Schänzel, L.-M., 2011. Coupled thermo-viscoplasticity of glassy polymers in the logarithmic strain space based on the free volume theory. Int. J. Solids Struct. 48 (13), 1799–1817.
Monk, P., 2003. Finite Element Methods for Maxwell's Equations. Oxford University Press, Clarendon.
O'Halloran, A., O'Malley, F., McHugh, P., 2008. A review on dielectric elastomer actuators, technology, applications, and challenges. J. Appl. Phys. 104 (7) (Art. no. 071101).
Pao, Y., 1978. Electromagnetic forces in deformable continua. In: Nemat-Nasser, S. (Ed.), Mechanics Today, vol. 4. Pergamon Press, New York, pp. 209–306.
Pelrine, R., Kornbluh, R., Joseph, J., 1998. Electrostriction of polymer dielectrics with compliant electrodes as a means of actuation. Sens. Actuator A: Phys. 64 (1), 77–85.

Pelrine, R., Kornbluh, R., Kofod, G., 2000a. High-strain actuator materials based on dielectric elastomers. Adv. Mater. 12 (16), 1223–1225.
Pelrine, R., Kornbluh, R., Pei, Q., Joseph, J., 2000b. High-speed electrically actuated elastomers with strain greater than 100%. Science 287 (5454), 836–839.
Plante, J.-S., Dubowsky, S., 2006. Large-scale failure modes of dielectric elastomer actuators. Int. J. Solids Struct. 43 (25–26), 7727–7751.
Reese, S., Govindjee, S., 1998. A theory of finite viscoelasticity and numerical aspects. Int. J. Solids Struct. 35, 3455–3482.
Simo, J.C., Hughes, T.J.R., 1998. In: Marsden, J., Sirovich, L., Wiggins, S. (Eds.), Computational Inelasticity. Springer.
Simo, J., Taylor, R., 1985. Consistent tangent operators for rate-independent elastoplasticity. Comput. Methods Appl. Mech. Eng. 48 (1), 101–118.
Spencer, A., 1971. Theory of invariants. In: Eringen, A.C. (Ed.), Continuum Physics. Academic Press, New York, pp. 239–353.
Steigmann, D.J., 2009. On the formulation of balance laws for electromagnetic continua. Math. Mech. Solids 14 (4), 390–402.
Steinmann, P., 2011. Computational nonlinear electro-elasticity–getting started: mechanics and electrodynamics of magneto- and electro-elastic materials. In: Ogden, R.W., Steigmann, D.J., CISM Courses and Lectures (Eds.), Mechanics and Electrodynamics of Magneto- and Electro-elastic Materials. Springer, Vienna.
Tiersten, H., 1971. On the nonlinear equations of thermo-electroelasticity. Int. J. Eng. Sci. 9.7, 587–604.
Toupin, R.A., 1956. The elastic dielectric. J. Ration. Mech. Anal. 5, 849–915.
Truesdell, C., Toupin, R., 1960. The classical field theories. III/1. In: Flügge (Ed.), Handbuch der Physik. Springer.
Vu, D.K., Steinmann, P., Possart, G., 2007. Numerical modelling of the non-linear electroelasticity. Int. J. Numer. Methods Eng. 70 (6), 685–704.
Wissler, M., Mazza, E., 2007. Electromechanical coupling in dielectric elastomer actuators. Sens. Actuator A: Phys. 138 (2), 384–393.
Wissler, M., Mazza, E., 2005. Modeling of a pre-strained circular actuator made of dielectric elastomers. Sens. Actuator A: Phys. 120 (1), 184–192.
Wriggers, P., 2001. Nichtlineare Finite-Element-Methoden. Springer, Ger. Berlin, p. 495.